University of Maribor

Faculty of Energy Technology

Journal of ENERGY TECHNOLOGY

Volume 14 / Issue 3

NOVEMBER 2021

www.fe.um.si/en/jet.html

Journal of
ENERGY TECHNOLOGY

JET

VOLUME 14 / Issue 3

Revija Journal of Energy Technology (JET) je indeksirana v bazah INSPEC© in Proquest's Technology Research Database.

The Journal of Energy Technology (JET) is indexed and abstracted in database INSPEC© and Proquest's Technology Research Database.

JOURNAL OF ENERGY TECHNOLOGY

Ustanovitelj / FOUNDER

Fakulteta za energetiko, UNIVERZA V MARIBORU /
FACULTY OF ENERGY TECHNOLOGY, UNIVERSITY OF MARIBOR

Izdajatelj / PUBLISHER

Fakulteta za energetiko, UNIVERZA V MARIBORU /
FACULTY OF ENERGY TECHNOLOGY, UNIVERSITY OF MARIBOR

Tehnični urednik / TECHNICAL EDITOR

Sonja Novak

Tehnična podpora / TECHNICAL SUPPORT

Tamara BREČKO BOGOVČIČ

Izhajanje revije / PUBLISHING

Revija izhaja štirikrat letno v nakladi 100 izvodov. Članki so dostopni na spletni strani revije - www.fe.um.si/si/jet.html / The journal is published four times a year. Articles are available at the journal's home page - www.fe.um.si/en/jet.html.

Cena posameznega izvoda revije (brez DDV) / Price per issue (VAT not included in price): 50,00 EUR

Informacije o naročninah / Subscription information: http://www.fe.um.si/en/jet/subscriptions.html

Lektoriranje / LANGUAGE EDITING

TAIA INT d.o.o.

Oblikovanje in tisk / DESIGN AND PRINT

Foto Colarič, Boštjan Colarič s.p.

Naslovna fotografija / COVER PHOTOGRAPH

Jurij AVSEC

Oblikovanje znaka revije / JOURNAL AND LOGO DESIGN

Andrej PREDIN

Ustanovni urednik / FOUNDING EDITOR

Andrej PREDIN

Izdajanje revije JET finančno podpira Javna agencija za raziskovalno dejavnost Republike Slovenije iz sredstev državnega proračuna iz naslova razpisa za sofinanciranje domačih znanstvenih periodičnih publikacij / The Journal of Energy Technology is co-financed by the Slovenian Research Agency.

Spoštovani bralci revije Journal of energy technology (JET)

Cena energije v svetu, še posebej v zadnjih nekaj mesecih, se zelo draži. Zato je zelo pomembno, da ima Slovenija lastne enote za proizvodnjo električne in toplotne energije in na zalogi vsaj nekaj lastno pridobljene energije za pogon vozil. Samo v tem primeru lahko imamo dolgoročno ugodno ceno energije, kajti brez nje gospodarstvo ne more biti konkurenčno. Tudi sedanja izkušnja kaže na dejstvo, da mora biti državna energetika čim bolj neodvisna. Na srečo v tem trenutku proizvajamo dobršen del električne energije, ki jo potrebujemo, s pomočjo jedrske elektrarne, termoelektrarne ter s pomočjo obnovljivih virov. Toplotna energija je zagotovljena delno v termoenergetskih napravah s sistemom daljinskega ogrevanja, delno pa tudi v lastnih termoenergetskih enotah. Ob lastni proizvodnji vodika bi lahko s pomočjo odpadne toplote, nekaj električne energije ter z uporabo obnovljivih virov pridobili dobršen del količin vodika, ki ga potrebujemo za transport. Za uspešno nadaljnje obratovanje naših energetskih sistemov potrebujemo seveda zelo strokovne vzgojno izobraževalne sisteme. V tem smislu nudi Fakulteta za energetiko uspešne učne programe, v okviru fakultete pa izdajamo tudi znanstveno revijo JET, namenjeno izobraževalnemu in raziskovalnemu delu. Prepričan sem, da bo tudi ta številka revije prinesla nova spoznanja.

Jurij AVSEC
odgovorni urednik revije JET

Dear Readers of the Journal of Energy Technology (JET)

The price of energy in the world, especially in the last few months, has become increasingly expensive. Therefore, it is very important that Slovenia has its own units for the production of electricity and heat, as well as a supply of at least some of its own energy for vehicle transport. This is the only way the country can ensure a long-term energy price that is favourable, since without such a favourable price, the economy cannot be competitive. Current experience also points to the fact that the state energy sector must be as independent as possible. Fortunately, at the moment Slovenia produces a significant part of the electricity it needs, with the help of a nuclear power plant, a thermal power plant and renewable sources. Thermal energy is provided partly through thermal energy devices with a district heating system, and partly also through the country's own thermal energy units. In the case of Slovenia's own hydrogen production, a significant part of the amount of hydrogen required for transport could be acquired with the help of waste heat, some electricity and also through the use of renewable sources. For the successful further operation of the country's energy systems, it goes without saying that highly professional educational systems are required. In this sense, the Faculty of Energy offers successful curricula, and within the Faculty we also publish a scientific JET journal intended for educational and research work. I am sure that this issue of the magazine will also bring new insights.

Jurij AVSEC
Editor-in-chief of JET

Table of Contents / Kazalo

Transient circuit simulation of arc-free current breaking by resistance rise

Časovno odvisna simulacija toka odklopnika brez obloka in naraščajočo upornostjo

Dareer Bin Khalid, Michael Rock and Luigi Piegari 11

Quality assessment of single pass steel corner welded joints

Ocenitev kvalitete enovarkovnih jeklenih kotnih zvarnih spojev

Zdravko Praunseis, Bojan Stergar, Iztok Brinovar 23

Comparative analysis of synchronous motors

Primerjalna analiza sinhronskih motorjev

Vasilija Sarac, Goce Stefanov, Dragan Minovski 37

Limestone purity as decisive factor for its consumption in flue gas desulphurization process

Čistost apnenca kot odločilni faktor njegove porabe v procesu razžvepljevanja dimnih plinov

Martin Bricl 47

Measurements of characteristics of an electric motor for an electric vehicle drive

Meritve karakteristik elektromotorja za pogon električnega vozila

Klemen Srpčič, Gregor Srpčič 57

Instructions for authors 73

Journal of Energy Technology

JET Volume 14 (2021) p.p. 11-22
Issue 3, November 2021
Type of article 1.01
www.fe.um.si/en/jet.html

TRANSIENT CIRCUIT SIMULATION OF ARC-FREE CURRENT BREAKING BY RESISTANCE RISE

ČASOVNO ODVISNA SIMULACIJA TOKA ODKLOPNIKA BREZ OBLOKA IN NARAŠČAJOČO UPORNOSTJO

Dareer Bin Khalid[ℜ1], Michael Rock[2] and Luigi Piegari[3]

Keywords: current breaking, ATP-EMTP, time-dependent resistance, optimisation, concave & convex functions.

Abstract

There has been intensive research and development in the field of Circuit breakers, whether DC and AC, or low voltage and high voltage. The result of this has led to the production of highly reliable circuit breakers that accompany a built-in arc extinguishing system. However, the purpose of this study is to give the basics for arc-free current breaking with fast interruption of fault currents, e.g., in surge protective devices (SPD) for AC and DC systems, by means of a time-dependent resistor with fast rising resistance. This investigation shall illustrate how the current can be driven almost to zero with a steadily time increasing resistance, and interrupted completely without an electric arc. The basic aim of the conducted transient circuit simulations is to determine suitable time functions for the current or resistance and necessary initial and final resistances. This paper will discuss the "optimisation conditions", a switching time as short as possible, small switch-off overvoltage, and possibly an energy conversion in the resistor as low as possible is set using ATP-EMTP and analytical calculations.

[1] Politecnico di Milano, Polimi, Dipartimento di Elettronica, Informazione e Bioingegneria, 20133 Milan, Italy, e-mail: dareerbin.khalid@mail.polimi.it, Technische Universität Ilmenau, 98693 Ilmenau, Germany, e-mail: dareerbin.khalid@tu-ilmenau.de

[2] Technische Universität Ilmenau, Department of Electrical Engineering and Information Technology, Group for Lightning and Surge Protection, 98693 Ilmenau, Germany, e-mail: michael.rock@tu-ilmenau.de

[3] Politecnico di Milano, Polimi, Dipartimento di Elettronica Informazione e Bioingegneria, Power Electronic Converters Electrical Machines and Drives, 20133 Milan, Italy, e-mail: luigi.piegari@polimi.it

Povzetek

Na področju odklopnikov, bodisi enosmernega ali izmeničnega toka, nizke ali visoke napetosti, poteka veliko raziskav, kar rezultira v proizvodnji zelo zanesljivih odklopnikov, ki spremljajo vgrajeni sistem za gašenje obloka. Namen tega članka je pokazati osnove za odklop električnega toka brez obloka s hitrimi prekinitvami okvarnih tokov, npr. v prenapetostnih zaščitnih napravah za izmenične in enosmerne sisteme s pomočjo časovno odvisnega upora s hitro naraščajočo upornostjo. Ta študija ponazarja, kako lahko električni tok prekinemo z enakomerno naraščajočo upornostjo in kako ga lahko popolnoma prekinemo brez električnega obloka. Glavni cilj izvedenih simulacij je določitev ustreznih časovnih funkcij za električni tok ali upor ter potrebne po začetnih in končnih upornostih. V članku so predstavljeni »optimizacijski pogoji«: čim krajši preklopni čas, majhna izklopna prenapetost, in morebitna čim nižja pretvorba energije v uporu, ki je določena z uporabo ATP-EMTP in analitičnih izračunov.

1 INTRODUCTION

In conventional switches (circuit-breakers), switching principles are applied based on electric arc interruption [1], [2]. The arc plasma, with its high temperature, intense radiation and stochastic behaviour, can lead to destruction, erosion and ageing. Arc-free switching, especially breaking of large currents with switching devices of equally small size is therefore desirable. Many considerations, especially in the DC sector, are given to power electronic switches or hybrid switches, which, however, usually require several "chop" switching operations [3]. Here, on the other hand, steady resistance increases $R(t)$ or $R(t,i(t))$ of a lumped solid resistor are to be investigated for switching off. Although this switching principle is supposed to be applicable for AC and DC as well as independent of the voltage level, the temporal resistance elevation corresponds to the so-called DC or low-voltage switching principle (current-limiting).

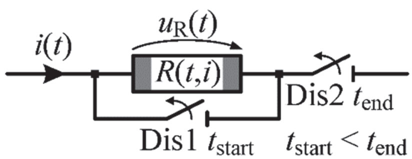

***Figure 1**: Schematic of switching device with time-dependent resistor*

For the defined start and end of the switching operation, the auxiliary switches in Fig.1 are recommended, exclusively, disconnectors (Dis1, Dis2) without breaking capacity. The conditions for these auxiliary switches are derived, and these are, in particular, the resistance values of the resistor at the start and at the end.

The basic question to be clarified is which continuous time function of resistance enables an ideal switch-off. This requires the solution of an optimisation task with regard to the switch-off overvoltage and the energy in the resistor.

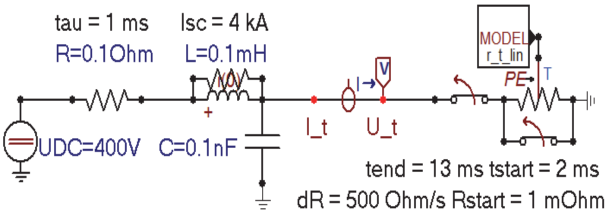

Figure 2: *Single-pole ohmic-inductive DC circuit for transient simulation in ATPDraw*

The study was carried out using analytical and numerical network analysis (Fig.2), using ATP-EMTP with ATPDraw interface [4] for circuit simulation.

2 PRINCIPLE OF OPERATION

The time-dependent resistance was simulated in ATP-EMTP with a TACS resistor, which is controlled by a time function programmed in MODELS [4]. Fig.3 shows a transient switch-off process with linearly increasing resistance in a DC circuit with a moderate time constant.

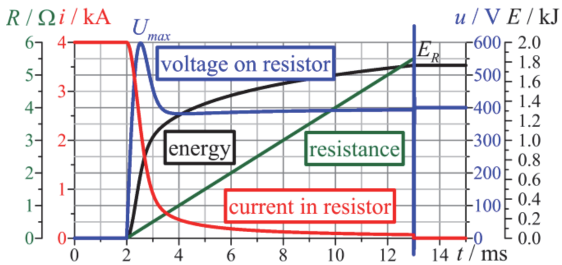

Figure 3: *Switching off with a linear rise of resistance in the ohmic-inductive DC circuit*

In order to allow a switch-off process to start from a steady-state operation and to be completed without numerical oscillations, the "switching conditions" must be considered in the numerical solution of the differential equation system (the trapezoidal rule used in ATP-EMTP).

2. 1 Conditions for opening of the first disconnector, Dis1

With reference to Fig.1, the closed disconnector Dis1 carries the current to be interrupted until the breaking process starts with the help of the resistor. This disconnector thus represents the low impedance bridging of the initial value R1 of the resistor.

Opening Dis1 at the instant start triggers the breaking process. To avoid ignition of an arc in the disconnector, the minimum arc voltage Uarc,min = 20 V to 40 V must be undercut when opening: $U_1 = R_1 \cdot I_1 < U_{arc,min}$. The limit value for the initial resistance R1 can be calculated with the instantaneous current I1 to be switched off: $R_1 \leq U_{arc,min}/I_1$. If the instantaneous current is not known, then the short-circuit current ISC in the circuit can be used for worst-case consideration: $R_1 \leq U_{arc,min}/I_{SC}$. Regardless of the voltage level, short-circuit currents are in the range ISC = 500 A … 50 kA.

e.g. $U_{arc,min}$ = 40 V I_{SC} = 4 kA → $R_1 \leq 10$ mΩ

e.g. $U_{arc,min}$ = 20 V I_{SC} = 20 kA → $R_1 \leq 1$ mΩ

Because of the small voltage U1 = Uarc,min and the finite voltage rise across the resistor, re-ignition of disconnector Dis1 is unlikely.

2. 2 Conditions for opening the second disconnector, Dis2

The current i(t), decreasing due to the increasing resistance R(t), flows through the closed disconnector Dis2. Because the current cannot become exactly zero with a finite resistance R(t) and an isolating clearance is to be established, disconnector Dis2 is necessary.

Opening Dis2 at time end is the final completion of the breaking process. Opening the disconnector Dis2 without igniting an arc is possible if the current i(t) falls below the minimum arc current Iarc,min = 0.5 A to 1 A. Since the resistance R(t), which increases with time, becomes much larger than the line impedance or short-circuit impedance, the necessary resistance value R2 for the minimum arc current Iarc,min can be estimated with the open-circuit voltage UOC = 100 V – 100 kV of the system: $R_2 \geq U_{OC}/I_{arc,min}$.

e.g. $I_{arc,min}$ = 0.5 A U_{OC} = 250 V → $R_2 \geq 0.5$ kΩ

e.g. $I_{arc,min}$ = 1 A U_{OC} = 11.6 kV → $R_2 \geq 11.6$ kΩ

With the small current, the voltages across the disconnector Dis2 and voltage across the resistor R(t) = R2 should also be small enough to prevent re-ignition and flashover.

3 TEST SETUP AND SIMULATIONS

A brief introduction was given regarding the software ATPDraw and ATP-EMTP, which is being used here to simulate a circuit that represents a short circuit current of different magnitudes. As shown in the circuit diagram reported in Fig.2, we have a DC source, a series resistor and an inductor. This series resistor is used to change the short circuit current magnitude, whereas the inductor is used for changing the time constant, or it can actually realise how different voltage levels can affect our system. Then there is a variable resistor, which is controlled using programmable MODELS [4]. This can be programmed for a resistance rise using a linear function as well as non-linear, i.e., quadratic, or exponential, and also to calculate multiple characteristics during this rise of resistance taking place.

3. 1 Model and resistance rise functions

The model is programmed with different resistance rise functions in order to identify the optimal one.

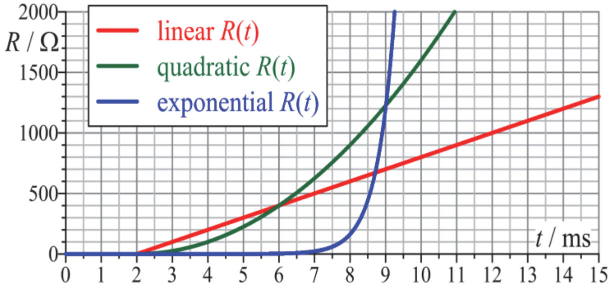

***Figure 4:** Output of different resistance rise with respect to time*

With linear resistance rise, even after a very long time, the final resistance is not very high. This is not very suitable, because, if we want to decrease and limit the high short circuit current near to zero, we need the resistance to be high enough so that there is no arc. This can be achieved with a high rate of resistance rise, but it will also create a high Umax, i.e., voltage across the Dis1 which will cause arcing, as well as may cause it to reclose. Using a quadratic function, the resulting resistance rise can be seen (Fig.4). This solves the problem of high Umax, since the resistance rise is slow at the start. Moreover, the resistance rise also reaches the desired value for the current limiting. The only issue here is that it takes a large time to reach that value. The exponential rise function gives the best result in terms of the resistance at the beginning of the current breaking process, as well as at the end. Since at the start when Dis1 in parallel to resistance opens, we need a small resistance so that the product with a high short circuit current results in a smaller Umax, but then an exponential rise to a high enough value that can limit the current to a near zero value easily in a short time, so that the overall stress on the system is minimal.

4 MATHEMATICAL MODELLING

The main goal is to achieve a time-based function for the variable resistance which enables ideal switch-off in the DC circuit, and which we can implement for all cases and scenarios. This requires the solution of an optimisation task regarding the switch-off time and the switch-off overvoltage.

4. 1 Time function based on Current

The optimisation goal is to search for an optimal time function of resistance R(t) to break a short circuit current. Therefore, instead of trying to model resistance functions in search of an optimum solution from them, we can work with the current functions.

$$U_{DC} = R_n \cdot i(t) + L_n \cdot \frac{di(t)}{dt} + R(t) \cdot i(t) \quad i(0) = \frac{U_{DC}}{R_n}$$

$$i(t) = \left(\frac{U_{DC}}{L_n} \cdot \int_0^t e^{-\int_0^T \frac{R_n + R(\vartheta)}{L_n} d\vartheta} dT + \frac{U_{DC}}{R_n} \right) \cdot e^{-\int_0^t \frac{R_n + R(T)}{L_n} dT}$$

However, these formulas are difficult to use for finding an optimal time course for breaking. What we can do is to replace our planned current breaking mechanism with another modelling and a controlled current source. Therefore, the search for the solution can be done by a predefined goal-function for i(t), as shown in Fig.5 below.

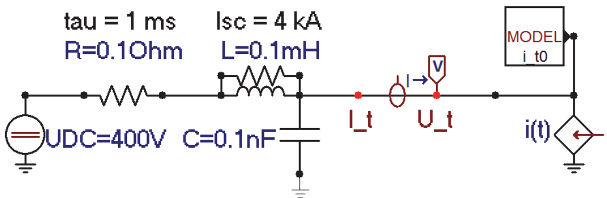

Figure 5: *ATPDraw circuit containing a current source controlled by a predefined current time function*

With the given time function of i(t) from tstart to the end above we can obtain tbreak. For the breaking voltage u(t) and its peak value on R(t) can be written:

$$u(t) = U_{DC} - R_n \cdot i(t) - L_n \cdot \frac{di(t)}{dt} \quad \rightarrow \quad U_{max}$$

The energy dissipated in resistance R(t) is:

$$E(t) = \int_0^t u(T) \cdot i(T)\, dT \;\rightarrow\; E_R = \int_0^{t_{break}} u(t) \cdot i(t)\, dt$$

There are many possible ways for the decrease of the short circuit current in a window from corner s to corner e according to Fig.6.

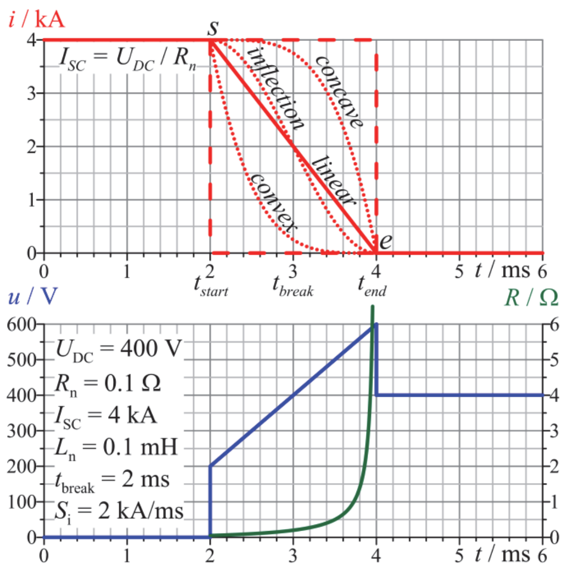

Figure 6: *Short circuit current decreasing in a time window and highlighted basic case linear decreasing current*

4. 2 Basic case

Analysing the linear decrease of i(t), where we have an initial high current, Rn·i(t) is high and constant current steepness over tbreak, Ln·di(t)/dt is not very high nor very low and the linear drop of current to zero (at s and e discontinuities) the function is:

$$i(t) = I_{SC} - S_i \cdot t \quad S_i = \frac{I_{SC}}{t_{break}} = \frac{U_{DC}}{R_n \cdot t_{break}} \quad I_{SC} = \frac{U_{DC}}{R_n}$$

$$i(t) = \frac{U_{DC}}{R_n} \cdot \left(1 - \frac{t}{t_{break}}\right) \quad u(t) = \frac{U_{DC}}{t_{break}} \cdot \left(t + \frac{L_n}{R_n}\right)$$

$$\Rightarrow \quad u(0) = \frac{U_{DC}}{t_{break}} \cdot \frac{L_n}{R_n} \quad t(U_{max}) = t_{break}$$

$$U_{max} = U_{DC} \cdot \left(1 + \frac{L_n}{R_n} \cdot \frac{1}{t_{break}}\right)$$

$$R(t) = \frac{u(t)}{i(t)} = \frac{R_n \cdot t + L_n}{t_{break} - t}$$

$$R(0) = L_n / t_{break} \quad R(t_{break}) \to \infty$$

$$\boldsymbol{E(t) = \frac{U_{DC}^2}{R_n} \cdot \frac{t}{t_{break}} \cdot \left(\frac{t}{2} + \frac{L_n}{R_n} \cdot \left(1 - \frac{t}{2t_{break}}\right) - \frac{t^2}{3t_{break}}\right)}$$

$$E_R = \frac{U_{DC}^2}{R_n} \cdot \left(\frac{1}{6} \cdot t_{break} + \frac{1}{2} \cdot \frac{L_n}{R_n}\right)$$

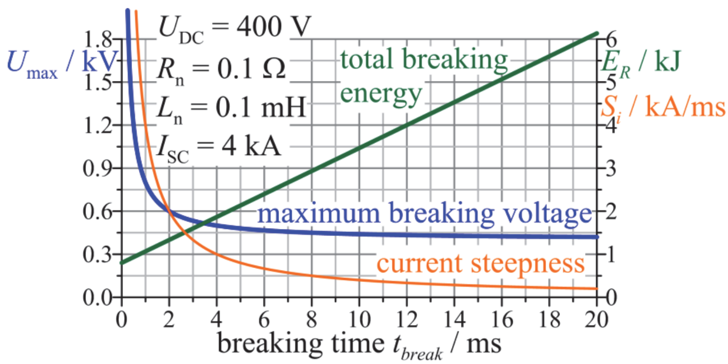

Figure 7: *Relation between maximum breaking voltage, total breaking energy, and breaking time for a linear decaying current*

Using fixed circuit parameters as shown in Fig.7, we obtained a relation between three important parameters for our study, Umax (on the y-axis left) and ER (on the y-axis right), with tbreak as the variable function. From this we can simply conclude that with increasing t_{break}, U_{max} tends to decrease, and ER increases, so we just have to find a common optimum solution.

4.3 Further cases

Using the same procedure as for the linearly decreasing current, many other current functions can be tested, and resistance functions can be calculated from them. Some selected suitable current functions are those listed below.

Concave quadratic function:

$$i(t) = \frac{U_{DC}}{R_n} \cdot \left(1 - \frac{t^2}{t_{break}^2}\right) \qquad R(t) = \frac{u(t)}{i(t)} = \frac{(R_n \cdot t + 2 \cdot L_n) \cdot t}{t_{break}^2 - t^2}$$

Convex quadratic function:

$$i(t) = \frac{U_{DC}}{R_n} \cdot \left(1 - \frac{t}{t_{break}}\right)^2$$

$$R(t) = \frac{R_n \cdot t \cdot (2 \cdot t_{break} - t) + 2 \cdot L_n \cdot (t_{break} - t)}{(t_{break} - t)^2}$$

Concave nth power function:

$$i(t) = \frac{U_{DC}}{R_n} \cdot \left(1 - \frac{t^n}{t_{break}^n}\right) \quad n = 1, 2, 3, \ldots \quad R(t) = \frac{(R_n \cdot t + n \cdot L_n) \cdot t^{n-1}}{t_{break}^n - t^n}$$

Convex nth power function:

$$i(t) = \frac{U_{DC}}{R_n} \cdot \left(1 - \frac{t}{t_{break}}\right)^n \quad n = 1, 2, 3, \ldots$$

$$R(t) = R_n \cdot \left(\frac{t_{break}}{t_{break} - t}\right)^n - R_n + \frac{n \cdot L_n}{t_{break} - t}$$

Concave exponential function:

$$i(t) = \frac{U_{DC}}{R_n} \cdot \left(e \cdot \left(1 - \frac{t}{t_{break}}\right) + 1 - e^{1 - \frac{t}{t_{break}}}\right)$$

$$R(t) = \frac{R_n \cdot e \cdot \left(t_{break} \cdot \left(e^{-\frac{t}{t_{break}}} - 1\right) + t\right) + L_n \cdot e \cdot \left(1 - e^{-\frac{t}{t_{break}}}\right)}{t_{break} + e \cdot t_{break} \cdot \left(1 - e^{-\frac{t}{t_{break}}}\right) - e \cdot t}$$

Convex exponential function:

$$i(t) = \frac{U_{DC}}{R_n} \cdot \left(e^{\frac{t}{t_{break}}} - e \cdot \frac{t}{t_{break}}\right)$$

$$R(t) = \frac{R_n \cdot e \cdot \left(t_{break} \cdot \left(1 - e^{\frac{t}{t_{break}}}\right) + t\right) + L_n \cdot \left(e - e^{\frac{t}{t_{break}}}\right)}{t_{break} \cdot e^{\frac{t}{t_{break}}} - e \cdot t}$$

Concave trigonometric function:

$$i(t) = \frac{U_{DC}}{R_n} \cdot cos\left(\frac{\pi}{2} \cdot \frac{t}{t_{break}}\right)$$

$$R(t) = \frac{R_n \cdot \left(1 - cos\left(\frac{\pi}{2} \cdot \frac{t}{t_{break}}\right)\right) + \frac{\pi}{2} \cdot \frac{L_n}{t_{break}} \cdot sin\left(\frac{\pi}{2} \cdot \frac{t}{t_{break}}\right)}{cos\left(\frac{\pi}{2} \cdot \frac{t}{t_{break}}\right)}$$

Convex trigonometric function:

$$i(t) = \frac{U_{DC}}{R_n} \cdot \left(1 - sin\left(\frac{\pi}{2} \cdot \frac{t}{t_{break}}\right)\right)$$

$$R(t) = \frac{R_n \cdot sin\left(\frac{\pi}{2} \cdot \frac{t}{t_{break}}\right) + \frac{\pi}{2} \cdot \frac{L_n}{t_{break}} \cdot cos\left(\frac{\pi}{2} \cdot \frac{t}{t_{break}}\right)}{1 - sin\left(\frac{\pi}{2} \cdot \frac{t}{t_{break}}\right)}$$

Trigonometric inflection point function:

$$i(t) = \frac{U_{DC}}{R_n} \cdot \frac{1}{2} \cdot \left(1 + cos\left(\pi \cdot \frac{t}{t_{break}}\right)\right)$$

$$R(t) = \frac{R_n \cdot \left(1 - cos\left(\pi \cdot \frac{t}{t_{break}}\right)\right) + \pi \cdot \frac{L_n}{t_{break}} \cdot sin\left(\pi \cdot \frac{t}{t_{break}}\right)}{1 + cos\left(\pi \cdot \frac{t}{t_{break}}\right)}$$

Using the current function and the voltage equation a formula of resistance was found, and also the formula for the energy dissipated in that resistance. After different trials and errors, we finalised the above-mentioned set of current functions, and then simulated them using our controlling factor this time i.e., the current breaking time, tbreak. With different values of tbreak we calculated for our functions the maximum overvoltage and the energy dissipated in the resistance.

4. 4 Results and Optimisation

In the Table below we have the ATP simulation results tabulated in terms of U_{max} and E_R at three different t_{breaks}.

Table 1: *ER and Umax for different functions at three different* t_{breaks}

U_{max} = 400 V, R_n = 0.1 Ω, L_n = 0.1 mH	t_{break} = 2 ms		t_{break} = 6 ms		t_{break} = 10 ms	
	U_{max} [V]	**E_R [J]**	**U_{max} [V]**	**E_R [J]**	**U_{max} [V]**	**E_R [J]**
quad convex	500	1226	411	2080	404	2933
exp convex	502	1241	413	2126	405	3010
trig convex	508	1237	413	2115	404	2985
trig inflection	572	938	425	1998	409	2798
cubic convex	600	1142	407	1828	401	2514
linear decrease	600	1334	466	2400	439	3466
trig concave	714	1237	504	2115	462	2985
exp concave	744	1241	514	2126	468	3010
quad concave	800	1226	533	2080	480	2933
cubic concave	1000	1142	600	1828	520	2514
pow10 convex	2000	938	666	1216	415	1493
pow10 concave	2399	938	1066	1216	800	1493

respect to maximum overvoltage, as this factor is very important for the resistance to become part of the main circuit. After this we chose three functions that had the least value for energy. These current decaying functions were cubic convex, quadratic convex and power 10 convex.

5 TESTING RESULTS

For our final trial we tested each one of our chosen functions one by one, by taking their evaluated equation for resistance and putting them into the ATP model circuit. Using the same circuit with controlled resistance MODELS, we implemented the functions obtained for the resistance as functions of time from the previous analysis.

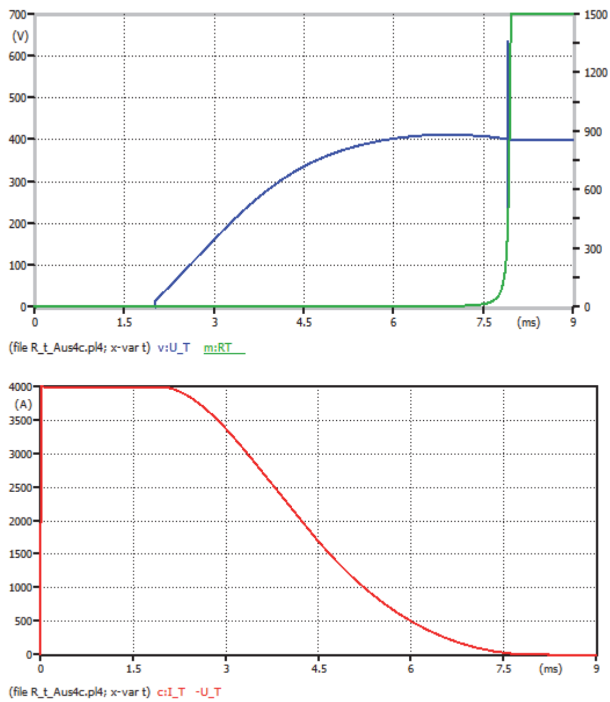

Figure 7: *Short circuit current (red) decreasing with increasing resistance (green) and behaviour of the voltage (blue)*

The results of one of our trials are given in Fig.7 where it can be seen that, with the increasing resistance the current is decreasing, but the time set here was for 6 ms, so itwas very smooth, and at t = 6 ms the resistance goes infinite, and the circuit opens.

So now these functions are dependent on t_{break}. Once the parallel switch, Dis1, will open at t_{start}, the second switch is programmed to open as soon as the current in the main circuit is less than or equal to 1 A, therefore fulfilling the condition of no arcing in the current breaking.

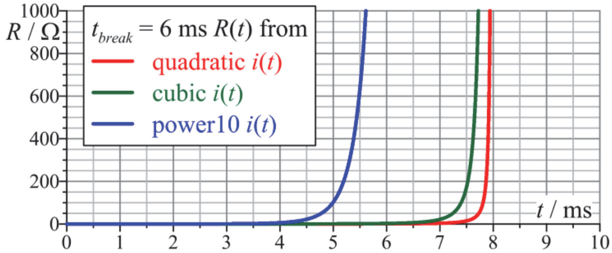

Figure 8: *Variable resistance rise using ATP with respect to time*

6 FUTURE SCOPE

To realise such resistances we need to perform further investigations and look into research related to different arrangements of controllable power-electronic switches, and the other being research related to the resistivity of different conducting, semi-conducting and superconducting materials.

Power Electronic devices, especially the controllable semiconductor switches with continuous voltage-current characteristic and switching characteristic, such as transistors, MOSFETs and IGBTs, can help us implement our resistance function. The parallel connection of several semiconductor switches serves to increase the current carrying capacity i.e., a short-circuit current.

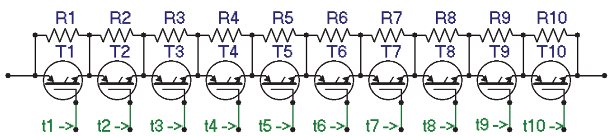

Figure 9: *Many power-semiconductor switches in switch-off mode, each with a parallel connected resistor in series*

With more stages in series the better the desired resistance-time or current-time function can be performed and the smaller the jumps, but the steady-state power dissipation or voltage drop at the operating current (and short-circuit current before the start of breaking)will be larger.

In terms of the resistivity of different materials, we can look into suitable conductors that exhibit a resistance time behaviour that is similar to the ones obtained in our results. Different alloys can also be shaped into forming a suitable resistance here for our case, depending upon their resistivity. The general rule is that resistivity increases with increasing temperature in conductors, and decreases with increasing temperature in insulators. It is also understood that when there is an increase in current, the temperature of the material it is flowing through will also increase, and therefore it is all related. Unfortunately, there is no simple mathematical function to describe these relationships displaying such behaviour of different metal alloys; the change in their resistivity with rise in temperature.

7 CONCLUSION

With the simulation of simple circuits in ATP-EMTP it can be shown that the interruption of small (open-circuit, operating) to large (short-circuit) electric currents can be realised arc-free. To do so we had to find a suitable variable resistance function and a schematic of operation. For the schematic part we just had to devise two switches with a coordination, and set some limiting conditions for current and voltage. However, an optimisation task had to be done for the part to find a suitable resistance function.

Thus, now, we have different resistance functions. But if we observe them closely, it can be said that all of these functions have similar shape, and, moreover, they are all analogous to the exponential resistance rise that we had found before. All three functions were shown to fulfil the aim of our study, and these resistances can be realised as shown in Figure 8.

References

[1] J.C. Das: *Transients in electrical systems analysis, recognition, and mitigation*, McGraw-Hill, 2010, New York.

[2 L.v.d. Sluis: *Transients in power systems*, John Wiley, 2001, Chichester.

[3] R. Lazzari, L. Piegari: *Design and implementation of LVDC hybrid circuit breaker*, IEEE Transactions on Power Electronics, Vol. 34, No. 8, August 2019, pp. 7369-7380.

[4] H.K. Høidalen, L. Prikler, F. Peñaloza: *ATPDRAW version 7.3 for Windows Users' Manual*, Rel. No. 1.0, May 2021. http://www.atpdraw.net/, https://www.emtp.org/

Nomenclature

(Symbols)	(Symbol meaning)
tbreak	Time taken to break open the circuit
ER	Energy dissipated by the resistor
Umax	Maximum voltage
Rn	Nominal resistance
Ln	Inductance

Journal of Energy Technology

JET Volume 14 (2021) p.p. 21-35
Issue 3, November 2021
Type of article 1.01
www.fe.um.si/en/jet.html

QUALITY ASSESSMENT OF SINGLE-PASS CORNER STEEL WELDED JOINTS

OCENITEV KVALITETE ENOVARKOVNIH JEKLENIH KOTNIH ZVARNIH SPOJEV

Zdravko Praunseis[1ℜ], Bojan Stergar[1], Iztok Brinovar[1]

Keywords: welded joints, microstructure, cracks, undercut, main frame

Abstract

The aim of this paper is to analyse the quality assessment of single-pass corner steel welded joints. The testing revealed the most burdened welded joints, which were cut out of the work-piece and prepared for metallographic macroscopic and microscopic analysis.

Thus, for all examinations of single-pass corner steel welded joints, the standard test procedures were used to determine the weldability and quality assessment of base materials and welded joints. Additionally, the effects of various welded defects of single-pass weld material on the bearing strength of corner welded joints will be analysed.

Povzetek

Bistvo članka je v analizi kvalitete enovarkovnih jeklenih kotnih zvarnih spojev. Preizkušanje zajema najbolj poškodovane dele zvarnih spojev, iz katerih so bili odvzeti vzorci za mikroskopske in makroskopske analize.

Za določitev varivosti in oceno kvalitete osnovnih materialov in zvarnih spoje so bile v raziskavi enovarkovnih kotnih zvarov uporabljene standardne metode. Ugotovljen je bil vpliv različnih va-

ℜ Corresponding author: Zdravko Praunseis, PhD, Associate Professor, Faculty of Energy Technology, University of Maribor, Tel.: +386 31 743 753, Fax: +386 7 6202 222, Mailing address: Hočevarjev trg 1, Krško, Slovenia, E-mail address: zdravko.praunseis@um.si

[1] Faculty of Energy Technology, University of Maribor, Hočevarjev trg 1, Krško, Slovenia

1 INTRODUCTION

With High-Strength Low-Alloyed Steels (HSLA) and their welded joints, the thermal and strain cycles during welding inevitably bring about metallurgical, mechanical and other heterogeneities. Fig. 1 and Fig. 2 show a summarised illustration of effects of various characteristics on fracture joint performance and/or fracture transition behaviours. Almost all of these factors result in the deterioration of the fracture performance of welded joints, [1,8].

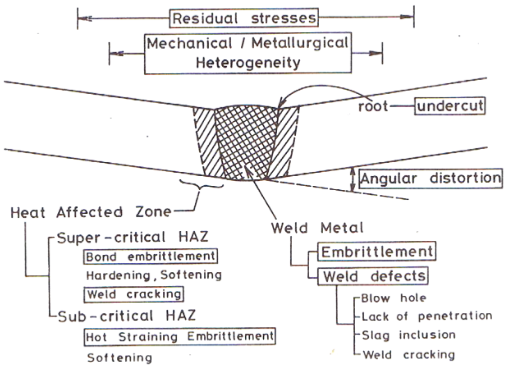

Figure 1: *Mechanical characteristics of energy steel welds*

Microstructures in welded joints of structural steels can be roughly divided as follows with regard to the change of material characteristics: (1) welded metal, (2) fusion line, (3) supercritical heat-affected zone (HAZ), and (4) subcritical HAZ. There are two main controlling factors that dominate the fracture performance of welded joints: factors controlling (a) fracture toughness and (b) deformation behaviour under loading. Although the fracture performance of welds is affected by various factors and their complex combined incidence, the following two controlling factors of brittle fracture strength of welds are essential: (I) the embrittlement in HAZ and the weld metal in the vicinity of pre-existing defects, and (II) inhomogeneity in strength, such as hardening and softening in HAZ and matching between the weld metal and base metal. The various factors control the embrittlement in welds. Mechanical heterogeneity is also a result of the same kind of controlling factors, [6,7]. In particular, as mentioned above, the embrittlement results in problems with the existence of local brittle zones (LBZs) in multi-pass welds.

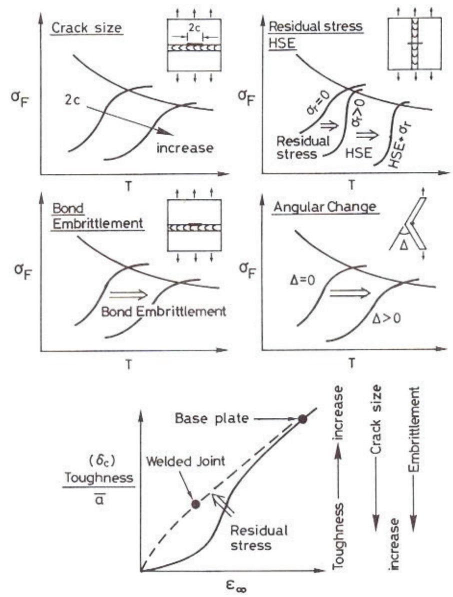

Figure 2: *Summary of various controlling factors on fracture performance of energy steel welds*

2 EXPERIMENTAL PROCEDURE AND DISCUSSION

Examination of single-pass corner welded joints of the main frame is carried out using the following standards methods:

- Surface inspection of welded defects at the single-pass welded joints (EN ISO 5817).

- Internal inspection of welded defects at the single-pass welded joints through microstructural supervision and measurement of microhardness (ISO 9051:2001, EN ISO 15614-1).

A visual surface inspection of welded defects at the single-pass welded joints demonstrates the presence of undercuts at the cap of the weld joints at marked places of the main frame from joint number 1 to joint number 5, as illustrated in Figures 3, 4 and 5 (see arrows) and Table 1.

The classification of defects (undercuts) in the single-pass corner welded joint is estimated in regard to the EN ISO 5817 standard (Tables 1 and 2).

The depths of the undercuts were measured using a laser depth micrometre and the results are shown in Table 2.

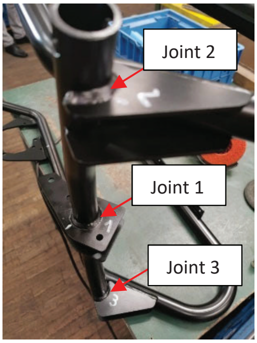

Figure 3: Inspected mark places of the main frame (Joints 1, 2 and 3)

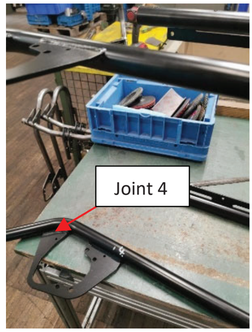

Figure 4: Inspected mark places of the main frame (Joint 4)

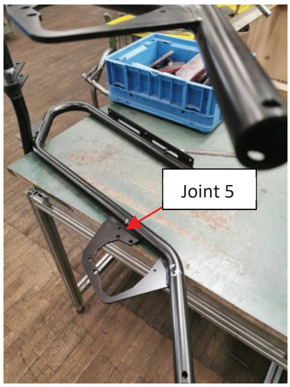

Figure 5: Inspected mark places of the main frame (Joint 5)

Table 1: *EN ISO 5817 standard classification of defects (undercuts) in a single-pass corner welded joint*

Defect sort	Drawing	Weld joint class D	Weld joint class C	Weld joint class B
Undercut at the cap of the weld joint.	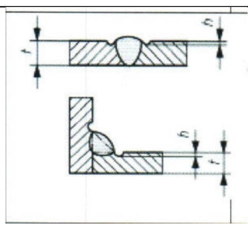 Base material thickness, t, from 0.5mm to 3.0mm.	A short undercut length is permitted based on the total length of the weld. h≤ 0.2 t	A short undercut length is permitted based on the total length of the weld. h≤ 0.1 t	An undercut length is not permitted.

The weld joint class is ordered by the constructor (designer) of the welded structure of the product, based on the estimated and achieved level of the thermal stresses, residual stresses and loading stresses that pertain to the constructed product. The highest level attained of the thermal stresses, residual stresses and loading stresses of a welded structure is typical for weld joint class B, while the lowest level attained of the thermal stresses, residual stresses and loading stresses of a welded structure is typical for weld joint class D. Thus, the main frame product investigated meets the standards of weld joint class D.

Table 2: *Measured and estimated values of undercuts in single-pass corner welded joints*

Joint Number	Weld class D	Weld class C
Joint 1 	Base material thickness, t=3mm Permitted undercut depth, h_a=0.6mm Measured undercut depth, h_m=0.2mm $h_m=0.2mm \le h_a=0.6mm$ Total length of weld, Lw=131mm Total length of undercut, L_u=12mm This equates to 9.1% of the total length of the weld. A short total undercut length (9.1%) is permitted in this length of weld.	Permitted undercut depth: h_a=0.3mm $h_m=0.2mm \le h_a=0.3mm$
Joint 2 	Base material thickness, t=3mm Permitted undercut depth, h_a=0.6mm Measured undercut depth, h_m=0.3mm $h_m=0.3mm \le h_a=0.6mm$ Total length of weld, Lw=94mm Total length of undercut, L_u=11mm This equates to 11.7% of the total length of the weld. A short total undercut length (11.7%) is permitted in this length of weld.	$h_m=0.3mm \le h_a=0.3mm$

To be continued

Continuation

Joint 3 	Base material thickness, t=3mm Permitted undercut depth, h_a=0.6mm Measured undercut depth, h_m=0.2mm h_m=0,2mm≤ h_a=0.6mm Total length of weld, Lw=58mm Total length of undercut, L_u=6mm This equates to 10.3% of the total length of the weld. A short total undercut length (10.3%) is permitted in this length of weld.	h_m=0.2mm≤ h_a=0.3mm
Joint 4 	Base material thickness, t=3mm Permitted undercut depth, h_a=0.6mm Measured undercut depth, h_m=0.2mm h_m=0.2mm≤ h_a=0.6mm Total length of weld, Lw=91mm Total length of undercut, L_u=9mm This equates to 9.8% of the total length of the weld. A short total undercut length (9.8%) is permitted in this length of weld.	h_m=0.2mm≤ h_a=0.3mm
Joint 5 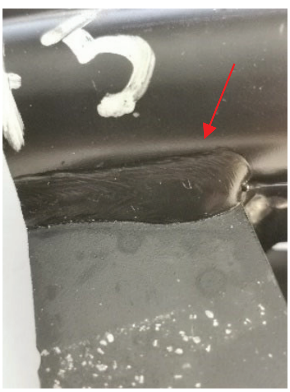	Base material thickness, t=3mm Permitted undercut depth allowed, h_a=0.6mm Measured undercut depth, h_m=0.1mm h_m=0,1mm≤ h_a=0.6mm Total length of weld, Lw=91mm Total length of undercut, L_u=3mm This equates to 3.2% of the total length of the weld. A short total undercut length (3.2%) is permitted in this length of weld.	H_m=0.1mm≤ h_a=0.3mm

A further stage of examinations involved an internal inspection of welded defects at the single-pass corner welded joints through microstructural supervision and measurement of microhardness.

For this purpose, five samples were cut out from the main frame (Figures 3, 4 and 5 (see arrows)) and marked 1 to 5. Metalographical samples were brushed, polished and etched with 5% nital (Figure 6). The etched samples were observed using an optical microscope in order to determine the microstructure and presence of cracks and microcracks and other typical welded defects. Microhardnes measuring (HV 0.1) was performed according to the ISO 9051:2001 standard with the aim of determining the local brittle zones (LBZ) with the highest hardness where cracks may appear.

Figure 6: Metalographical samples used for determination of microstructure and microhardness measurements at the single-pass corner welded joints

The results of the tests to measure the microhardness of weld metal and the HAZ at the single-pass corner welded joints are shown in the final report (Figure 7).

The highest value of 259 HV 0.1 was measured in the HAZ of the single-pass corner welded joints (Figure 7), which is much lower than the maximum permitted microhardness value (340 HV) in the welded joint with a carbon content lower than 0.22%, according to the EN ISO 15614-1 standard.

Microhardness Test Results

Faculty of Energy Technology
Laboratory for Energy Management and Engineering
Hocevarjev trg 1

3.9.2021 12:53, Page 1

Test Program	Single pass filled Corner weld joint		
Limits for :	Nominal Value	Upper tolerance limit	Lower tolerance limit
WM-FL-HAZ	0,00	300,00	150,00

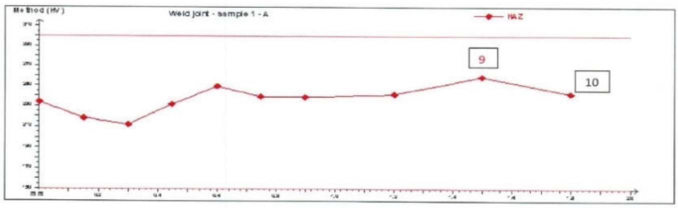

Number	Hardness value	Conversion	Date	Time	Operator	Comment
HAZ						
1	233,8 HV 0,1	-	3.9.2021	12:53:26	FELABEMI	
2	218,5 HV 0,1	-	3.9.2021	12:53:31	FELABEMI	
3	212,1 HV 0,1	-	3.9.2021	12:53:36	FELABEMI	
4	231,7 HV 0,1	-	3.9.2021	12:53:39	FELABEMI	
5	249,4 HV 0,1	22,0 HRC	3.9.2021	12:53:43	FELABEMI	
6	239,5 HV 0,1	20,3 HRC	3.9.2021	12:53:48	FELABEMI	
7	238,8 HV 0,1	-	3.9.2021	12:53:56	FELABEMI	
8	241,8 HV 0,1	20,7 HRC	3.9.2021	12:54:02	FELABEMI	
9	259,0 HV 0,1	23,8 HRC	3.9.2021	12:54:16	FELABEMI	
10	242,5 HV 0,1	20,9 HRC	3.9.2021	12:54:29	FELABEMI	

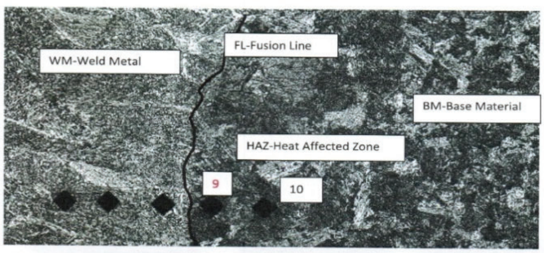

Seite - 1 -

Figure 7: Microhardness test results of the weld metal and HAZ at the single-pass corner welded joints

Carbon equivalents for theorethical prediction of microcracks and weldability of single-pass corner welded joints are calculated according to the EN 1011-2 standard using the equation (2.1), in regard to the real chemical composition of the base material (steel tube and steel plate) and weld metal of the single-pass corner welded joints, measured using an X-ray fluorescence spectrometer XRF (Thermo Scientific Niton XL3t GOLDD+), as illustrated in Table 3.

$$\mathrm{Ceq} = \mathrm{C} + \frac{\mathrm{Mn}}{6} + \frac{\mathrm{C_r} + \mathrm{M_o} + \mathrm{V}}{5} + \frac{\mathrm{N_i} + \mathrm{C_u}}{15} \qquad (2.1)$$

Table 3: *Real chemical composition of base material (steel tube and steel plate) and weld metal of single-pass corner welded joint, measured using an X-ray fluorescence spectrometer XRF (Thermo Scientific Niton XL3t GOLDD+) and values of calculated C_{eq} according to the EN 1011-2 standard:*

Chemical Composition (%)	C	Si	Mn	P	S	Cr	Ni	Mo	Cu	V
Steel tube	0.169	0.201	1.354	0.129	0.038	-	-	-	-	0.021
Steel plate	0.081	0.006	0.732	0.011	0.002	0.018	0.007	0.003	0.006	
Consumable VAC 65	0.078	1.110	1.564	0.020	0.025	0.002				
Weld metal (WM)	0.101	0.184	1.421	0.010	0.029	0.009	0.001	0.002	0.005	0.019
Carbon equivalent (C_{eq})	$C_{eqBM\ (tube)}$ = 0.398	$C_{eqBM\ (plate)}$ = 0.208	C_{eqWM} = 0.343							

The values of the calculated carbon equivalent (C_{eq}) predict the following appearance of microcracks in single-pass corner welded joints:

If $C_{eqBM\ (tube)} = 0.398 > C_{eqWM} = 0.343$, cold microcracks may appear in the base material.

If $C_{eqBM\ (plate)} = 0.208 < C_{eqWM} = 0.343$, cold microcracks may appear in weld metal.

In the event that the calculated $C_{eqBM\ (tube)} = 0.398$ and $C_{eqWM} = 0.343$ is lower than 0.40, this value guarantees very good weldability of the base material steel plate and tube used for welding of the main frame.

Due to the possibilty of the appearance of cold microcracks in weld metal and base material, an investigation into the microstructure of single-pass corner welded joints was carried out using an optical microscope (Figures 8, 9, 10, 11, 12 and 13).

Cracks and microcracks in combination with undercut can be very dangerous for the safe operation of single-pass corner welded joints, due to the concentration of stress that can appear around the profile of undercuts, thus a further investigation into the microstructure of single-pass corner welded joints is required.

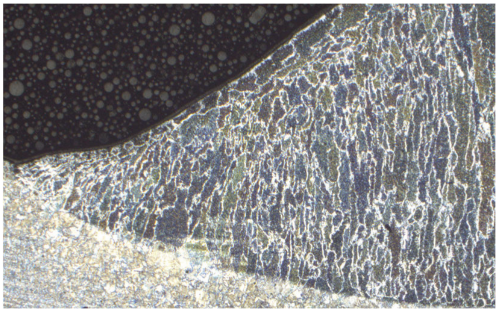

Figure 8: Microstructure without the presence of cracks in the weld metal, and the HAZ of a single-pass corner welded joint (sample 1, joint 1), mag(50x).

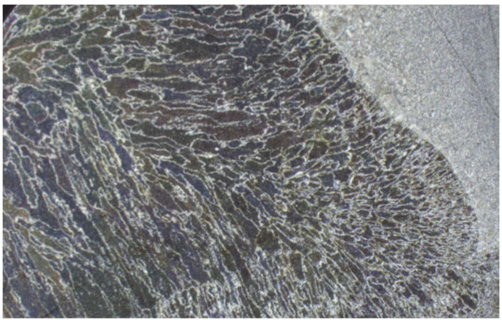

Figure 9: Microstructure without the presence of cracks in the weld metal, and the HAZ of a single-pass corner welded joint (sample 2, joint 2), mag(50x).

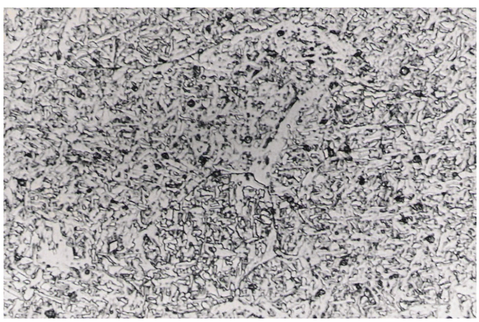

Figure 10: Ferritic-perlitic microstructure without the presence of cracks in the weld metal of a single-pass corner welded joint (sample 3, joint 3), mag(100x).

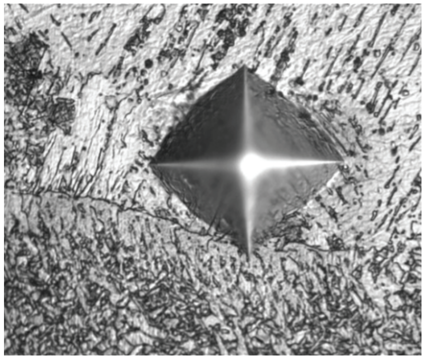

Figure 11 : Bainitic-martenzite coarse grain microstructure at the point where the highest level of microhardness (259 HV) was measured, without the presence of cracks of the HAZ of a single-pass corner welded joint (sample 3, joint 3), mag(200x).

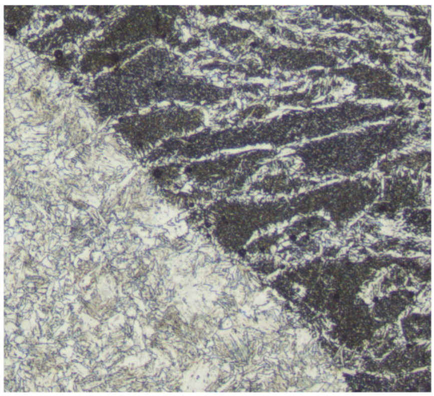

Figure 12: Microstructure without the presence of cracks in the weld metal, and the HAZ of a single-pass corner welded joint (sample 4, joint 2), mag(75x).

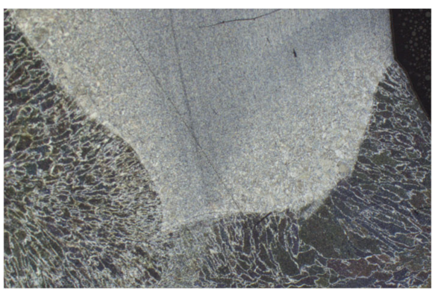

Figure 13: Microstructure without the presence of cracks in the weld metal, and the HAZ of a single-pass corner welded joint (sample 5, joint 5), mag(50x).

The investigations in the microstructure of single-pass corner welded joints confirmed that in all single-pass welded joints, weld metal and the HAZs, cracks and microcracks did not appear due to the proper selection of base materials, consumables and welding technology.

3 CONCLUSIONS

This examination of single-pass corner welded joints of the main frame resulted in the following conclusions:

1. Classification of defects (undercuts) in single-pass corner welded joints was estimated based on the EN ISO 5817 standard, which permitted existing undercuts in real single-pass corner welded joints in the case of weld joint class D and weld joint class C.

2. The highest value of 259 HV 0.1 was measured in the coarse grain heat-affected zone (CG HAZ) at the single-pass corner welded joints (Figure 7), which is much lower than the maximum permitted microhardness value (340 HV) in the welded joint with a carbon content lower than 0.22%, according to the EN ISO 15614-1 standard. This value of 259 HV 0.1 guarantees that dangerous cracks, microcracks or any other typical welded defects do not form in single-pass corner welded joints.

3. The investigations into the microstructure of single-pass corner welded joints confirmed that in all single-pass welded joints, weld metal and HAZs, cracks and microcracks, as well as other typical welded defects, did not appear due to the proper selection of base material, consumables and welding technology.

Acknowledgements

The authors would like to thank the company Skitii d.o.o. Izlake, Slovenia for supplying the material used for welding.

References

[1] **Z. Praunseis:** *The influence of Strength Under-matched Weld Metal containing Heterogeneous Regions on Fracture Properties of HSLA Steel Weld Joint* (Dissertation in English). Faculty of Mechanical Engineering, University of Maribor, Slovenia, 1998

[2] BS 5762, *Methods for crack opening displacement (COD) testing,* The British Standards Institution, London 1979

[3] ASTM E 1152-87, *Standard test method for determining J-R curves,* Annual Book of ASTM Standards, Vol. 03.01, American Society for Testing and Materials, Philadelphia, 1990

[4] ASTM E 1290-91, Standard test method for crack-tip opening displacement (CTOD) fracture toughness measurement, American Society for Testing and Materials, Philadelphia, 1991

[5] GKSS Forschungszentrum Geesthacht GMBH, *GKSS-Displacement Gauge Systems for Applications in Fracture Mechanic*

[6] **Z. Praunseis, M. Toyoda, T. Sundararajan**: *Fracture behaviours of fracture toughness testing specimens with metallurgical heterogeneity along crack front.* Steel res., Sep. 2000, 71, no.9

[7] **Z**. **Praunseis**, **T. Sundararajan, M. Toyoda, M. Ohata:** *The influence of soft root on fracture behaviors of high-strength, low-alloyed (HSLA) steel weldments.* Mater. manuf. process., 2001, vol. 16, 2

[8] **M. Toyoda**: *Fracture toughness evaluation of steel welds.* Book of Projects, Osaka University, 1989

Journal of Energy Technology

JET Volume 14 (2021) p.p. 35-45
Issue 3, November 2021
Type of article 1.01
www.fe.um.si/en/jet.html

COMPARATIVE ANALYSIS OF SYNCHRONOUS MOTORS

PRIMERJALNA ANALIZA SINHRONSKIH MOTORJEV

Vasilija Sarac[ℜ], Goce Stefanov[1], Dragan Minovski[1]

Keywords: FEM models, synchronous motors, steady-state characteristics, transient characteristics

Abstract

This paper compares the parameters, steady-state and transient characteristics of two different types of synchronous motors (SM) – a motor with surface mounted magnets on the rotor, and a motor with embedded magnets and squirrel cage winding, widely known as a line-start synchronous motor. The comparison is based on results obtained from analytical, numerical and transient models of both motors for the same output power of the motors. The models for obtaining transient characteristics allow comparison of acceleration of both motors taking into consideration that the line-start SM is a self-starting motor while the SM with surface magnets is always started with the aid of a PWM inverter. The results obtained from the analytical, numerical and transient models of the motors should assist in choosing the most cost-effective solution in terms of the type of the motor for the appropriate application.

Povzetek

V članku je predstavljena primerjava parametrov, ustaljene in tranzientne karakteristike dveh različnih tipov sinhronih motorjev (SM) – motorja s površinsko nameščenimi trajnimi magneti ter motorja z vgrajenimi trajnimi magneti in kratkostično kletko. Primerjava temelji na pridobljenih rezultatih iz analitičnega, numeričnega in tranzientnega modela obeh motorjev pri enaki izhodni moči motorjev. Modeli za določitev tranzientnih karakteristik omogočajo primerjavo hitrosti obeh motorjev upoštevajoč, da je SM s trajnimi magneti in kratkostično kletko samozagonski motor, medtem ko se

[ℜ] Corresponding author: Prof. Vasilija Sarac, University Goce Delcev, Faculty of Electrical Engineering, Krste Misirkov 10-A, 2000 Stip, North Macedonia, Tel: +389 32 550 650, E-mail address: vasilija.sarac@ugd.edu.mk

[1] University Goce Delcev, Faculty of Electrical Engineering, Krste Misirkov 10-A, 2000 Stip, North Macedonia

SM s površinsko nameščenimi trajnimi magneti vedno zažene s pomočjo PWM pretvornika. Rezultati prej omenjenih modelov motorjev naj bi bili v pomoč pri izbiri stroškovno najugodnejše rešitve s stališča tipa motorja za določeno aplikacijo.

1 INTRODUCTION

Finding an adequate type of motor for certain applications is not an easy task for electrical engineers. There are varieties of induction motors, which nowadays are often used in various drive applications. The development of power electronics has made this choice even harder. Until recently, the three-phase asynchronous motor has dominated in the industries' drive system due to its robustness, low price and low maintenance costs. The power electronics facilitates its operation in variable speed drives, as the speed of this type of motor (asynchronous motor) can be easily regulated by frequency inverters. However, the low efficiency and the low power factor remain one of the major drawbacks of this type of induction motor. In contrast, synchronous motors have a high efficiency and power factor, which make them a main competitor of asynchronous motors. However, the choice of the most cost-effective solution in terms of motor type in a specific application is not so simple. Synchronous motors can be divided into two major groups – motors without cage winding on the rotor, and with various geometries of the magnets mounted on the rotor surface or embedded inside the rotor. This type of synchronous motor cannot be started without the aid of voltage inverters, i.e. they are not self-starting motors or they cannot be started directly from the mains power supply. Therefore, the cost of the motor rises as the cost of the inverter must be added to the cost of the motor. The second group of synchronous motors is the line-start synchronous motor with a design very similar to that of the asynchronous squirrel cage motor. The only difference in construction from the asynchronous squirrel cage motor is the magnets embedded inside the rotor. The squirrel cage winding assists in motor starting while the magnets pull the motor into synchronism. In an era where energy efficiency is of paramount importance, it is understandable why there has been increased interest in synchronous motors in the scientific community. The control theory, including sensorless speed control based on different original control techniques for improving the speed regulation of synchronous motors with surface or embedded magnets, is analysed in [1]-[3]. Another field of research is the losses of synchronous motors [4]. The early detection of motor faults by monitoring the stator currents or derating the motor due to a broken bar fault was studied in [5]-[6]. An in-depth analysis of motor losses can be found in [5]. Not just faults are those that limit the motor operation and life expectancy. Noise and vibration often accompany operation of the motor. The choice of the most adequate combination of the number of slots and number of poles can reduce noise and vibration, and make operation of the motor smoother [7]. Synchronous motors have wide application in the automotive industry, e.g. in high-speed applications. A detailed study of the transient characteristics of an induction motor with copper and aluminium bars in high-speed applications can be found in [8]. Another aspect of usage of synchronous motors in high-speed applications is the mechanical design of the rotor in terms of the reduction of mechanical stress. An in-depth study of the mechanical construction of the rotor with surface and embedded magnets in terms of the mechanical stress can be found in [9]. Another issue that arises in terms of the operation of synchronous motors is the harmonics that are often present when a synchronous motor is operated by an inverter [10]. The literature review undertaken for this research showed that very few papers address the comparison between synchronous motors with surface mounted magnets (SMSPM) and line-start synchronous motors (LSSPMM). This comparison is interesting from a design point of view as well as from the point of view of the operating characteristics of the motors. Three different methodologies were used for developing the motor models and obtaining the operating characteristics – a computer model for analytical calculation of parameters and steady state characteristics, a numerical model for magnetic flux density distribution, and a dynamic model for obtaining the transient characteristics. Both motors were constructed for the same power output and with minimum material consumption (copper and permanent magnets), which allowed maximum efficiency and power factor to be obtained. The results obtained from all three methods were compared and adequate conclusions were derived. The comparison shown should assist in finding an adequate motor for certain applications by taking into consideration all the advantages and drawbacks of the analysed motors.

2 METHODOLOGY AND RESULTS

2. 1 Computer models for analytical calculation of parameter and steady-state characteristics

Ansys software was used in modelling the computer models of both synchronous motors, which allows calculation of motor parameters and operating characteristics. Both types of synchronous motors were derived from the asynchronous motor type 2AZ155-4 or the new model of motor-5AZ100LA-4, produced by the Croatian company Rade Končar [11]. Both synchronous motors were modelledwith one constraint: the output power should remain unchanged, i.e. 2.2kW, the same as the asynchronous motor. In order for the computer models to reach a solution and provide accurate results, the exact geometry of the motors must be defined as well as all the materials used in construction of the motor. A cross-section of both motors is presented in Fig.1. The output results from the computer models are the motor parameters at rated load, no load and locked rotor, as illustrated in Table 1. The comparison of these two types of synchronous motors is justified by the fact that in spite of their quite different rotor configuration, both motors do not exhibit any Joule's losses in the rotor.

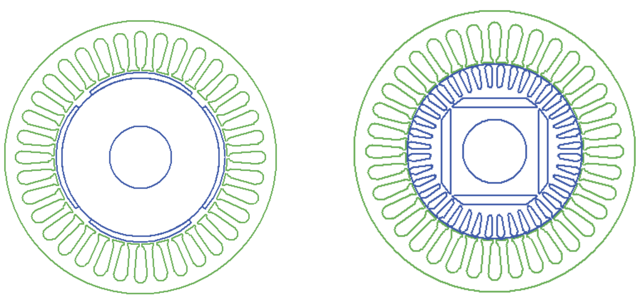

a) b)

Figure 1: *Cross-section of the analysed motors*

Table 1: *Parameters and operating characteristics of analytical model*

Parameters	SMSPM	LSSPMM
Stator phase resistance R_1 (Ω)	2.95	1.8
Number of conductors per slot	125	97
Wire diameter (mm):	0.8	0.9
Stator slot fill factor (%):	70	69.9
Stator copper weight (kg):	3.91	3.83
Permanent magnet weight (kg):	0.61	0.5
Armature core steel weight (kg)	4.4	4.4
Rotor core steel weight (kg):	3.7	2.7
Rotor winding weight (kg)	/	0.61
Total net weight (kg):	12.6	12.1
Maximum output power (W)	6,113	5,764
Rated load operation		
Armature current (A)	3.56	3.52
Input power (W)	2,349	2,303
Output power (W)	2,200	2,199
Frictional & windage loss (W):	22	22
Iron-core loss (W):	14.2	13.9
Armature copper loss (W)	112.2	68
Total loss (W):	148.4	104
Efficiency (%)	93.7	95.5
Rated speed (rpm)	1,500	1,500
Rated torque (Nm)	14	14
Power factor (/)	0.996	0.992
Torque angle (°)	18.5	69.3
Locked rotor operation		
Start Torque (Nm)	/	62
No-load operation		
No-Load Line Current (A)	0.27	1.76
No-Load Input Power (W)	36.9	53

The SMSPM does not have any rotor winding so no losses are associated with it. At LSSPMM there is no current induced in the rotor winding when motor operates at a synchronous speed and no losses are associated with this winding. The predefined motor parameter is the output power which should remain unchanged. Both motors are derived from the three-phase asynchronous squirrel cage motor by redesigning the rotor. The same materials are used in both the motor configurations as in the original asynchronous motor. The same type of magnets are used in both motors. In order to achieve similar operating characteristics, the stator winding of the SMSPM has to be modified, i.e. the number of conductors per slot is increased. The programme automatically reduces the wire diameter in order to maintain the same slot fill factor, i.e. to maintain the same output power of the motor while not exceeding the limited slot fill factor of 75%. The increased number of conductors per slot increases the winding resistance and consequently the armature copper losses are higher in the SMSPM compared to the LSSPMM. Since all the other losses are almost the same, this increase of copper losses reduces the efficiency of the LSSPMM compared to the SMSPM. Both motors have almost the same power factor. The net weight and consumption of material are somewhat higher in the SMSPM. In terms of the maximum output power, both motors have satisfactorily high values, i.e. the overloading capability of both motors is almost the same and is sufficiently high, i.e. the ratio of breakdown torque to rated torque is 2.8 in the SMSPM and 2.62 in the LSSPMM. The motor current and efficiency for the various torque angles are presented in Fig. 2 and 3 respectively. The results in both the aforementioned figures should verify the data in Table 1 and illustrate the operation of both types of motors. The adequate values of the torque and efficiency can be read for the appropriate torque angle which defines the rated operation of the motor.

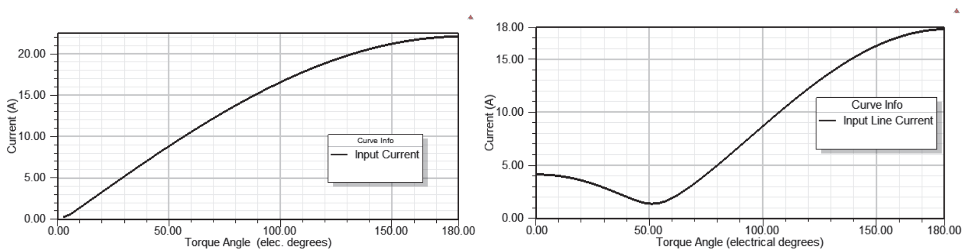

a) SMSPM b) LSSPMM

Figure 2: *Line current*

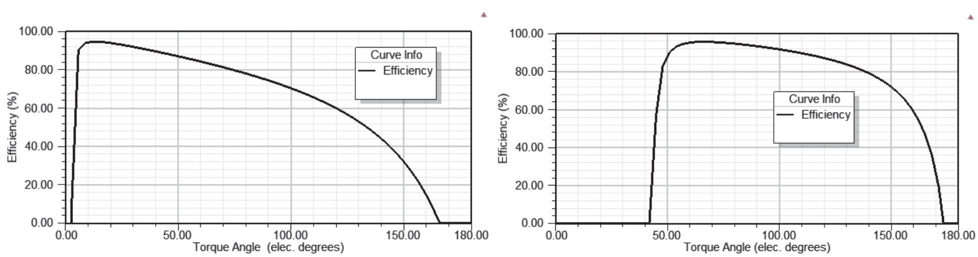

a) SMSPM b) LSSPMM

Figure 3: *Efficiency factor*

2. 2 FEM Model for numerical calculation of flux density

The FEM models of the electrical machines have become part of the standardised procedure for the design of motors. There are several rreasons for this: availability of various commercial or non-commercial programmes for creating FEM models of the machines, the importance of detection of areas of the cross-section of the motor with the high flux density, and detecting the need of machine redesigning if there are large areas of the machine cross-section with the high flux density. For both the analysed motors, FEM models were created for calculating the flux density distribution inside the motors. The results obtained are shown in Fig. 4.

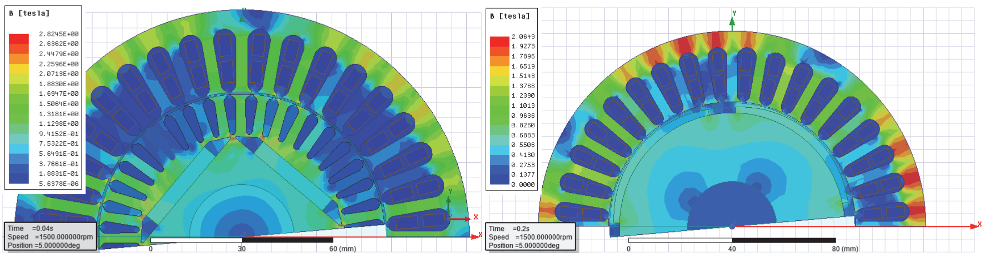

a) LSSPMM b) SMSPM

Figure 4: *Flux density distribution*

As can be seen from the results illustrated in Fig.4, the critical parts in the motor construction in the case of the LSSPMM are the edges of the flux barriers near to the rotor slots. One solution could be to alter the design of the rotor slots in order to provide a thicker magnetic core in this part of the motor. For both motors, the high flux density in stator yoke can be decreased by increasing the motor outer diameter. This could form part of an additional analysis as both the motors were derived from a three-phase asynchronous squirrel cage motor without changing the outer dimension of the motor or the original geometry and material of the stator laminations.

2. 3 Dynamic models and transient characteristics

The analysis of the motors' dynamics covers the transient characteristics of the speed, torque or current during acceleration of the motors up to steady-state operation. Although starting of these two types of synchronous motors is different, i.e. the LSSPMM is started directly from the mains while the SMSPM only required an inverter to start, an analysis of their transient characteristics is necessary in order to obtain data relating to their starting time, synchronisation and possibility to drive various loads. The dynamic model of the LSSPMM is simulated in Ansys while that of the SMSPM is simulated in Simulink. Both the motors were loaded with a step load of 14Nm, 0.35 seconds after the motor was started. The obtained transient characteristics of speed, torque and current are presented in Figs. 5, 6 and 7.

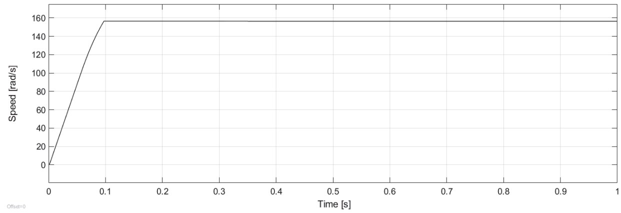

a) SMSPM

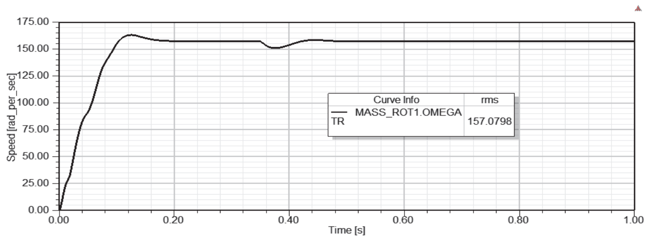

b) LSSPMM

Figure 5: *Transient characteristics of speed*

As can be seen from the illustrated transient characteristics of speed, the acceleration time of both motors is nearly the same and they achieved a synchronous speed of 1,500rpm or 157.07 rad/s. Both motors maintained the synchronous speed after they were loaded with the load torque.

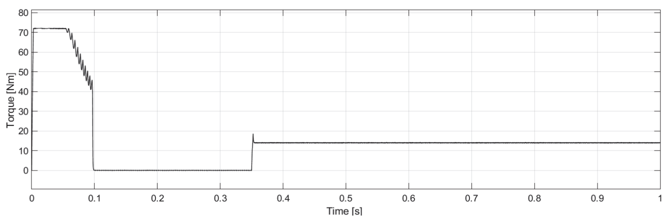

a) SMSPM

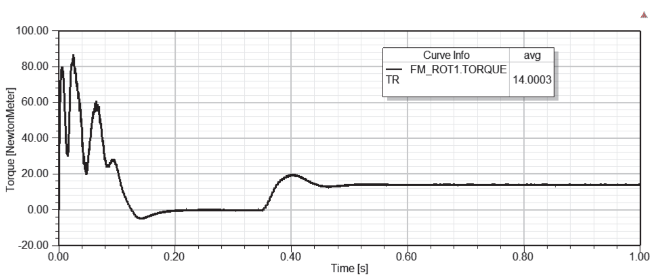

b) LSSPMM

Figure 6: *Transient characteristics of torque*

In both motors, the output torque after the acceleration has finished, reaches the no-load torque. After the step load of 14Nm is coupled to the motor shaft, the output torque reaches 14Nm.

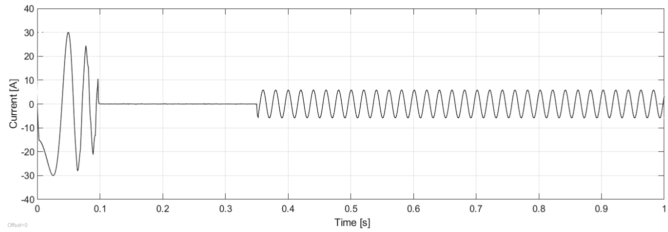

a) SMSPM

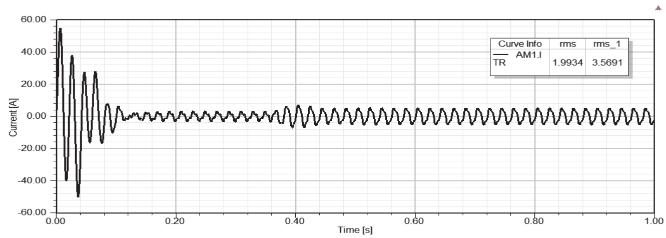

b) LSSPMM

Figure 7: *Transient characteristics of current*

From the transient characteristic of current of the SMSPM, after acceleration, the current reaches almost zero value which correlates with the data in Table 1 for the no-load current of 0.27A. After the step load of 14Nm is coupled to the motor shaft, the current increases to the rated current 4A (rms) and correlates with the analytical result of 3.5A. A similar observation can be derived for the current of the LSSPMM.

3 CONCLUSION

This paper describes an anaylsis of an LSSPMM and SMSPM. In terms of efficiency and material consumption, the LSSPMM has an advantage over the SMSPM, while the SMSPM has a greater overloading capability. Construction of the SMSPM is simple, however there is an ever-present danger of demagnetisation of the magnets due to the surface placement on the rotor. As the magnets are glued to the rotor, there is often a need to 'bandage' them to protect them from hazard at high speeds. The design of the rotor of the LSSPMM is more complicated, but the risk of demagnetisation of the magnets is lower as they are embedded inside the rotor and there is no need to 'bandage' them. In terms of simplicity of operation, the advantage of the LSSPMM is that it is self-starting and does not require an inverter in contrast to the SMPSM. However, in high-speed applications and electrical mobility, synchronous motors with surface magnets are often present and due to their isotropic rotor, the d- and q-axis inductances are identical and the saliency ratio (ξ = Lq/Ld) is 1. Therefore, no reluctance torque occurs. There is no straightforward answer as to which type of the two analysed motors is better. Each motor should be evaluated in terms of its specific application.

References

[1] **M. Štulrajter, V. Hrabovcová. M Franko**: *Permanent magnet synchronous motor control strategies*, Journal of Electrical Engineering, Vol.58, Iss.2, p.p. 79-84, 2007

[2] **E. Ojionuka, I. Chinaeke-Ogbuka, C. Ogbuka, C. Nwosu**: *Simplified sensorless speed control of permanent magnet synchronous motor using model reference adaptive system*, Journal of Electrical Engineering, Vol.70, Iss.6, p.p.473-479, 2019

[3] **G. Park, G. Kim, B-G. Gu:** *Sensorless PMSM inductance estimation based on the data drive approach,* Electronics, Iss.10, pp.1-19, 2021

[4] **P. Hudák, V. Hrabovcová, P. Rafajdus, J. Mihok:** *Core loss analysis of the reluctance synchronous motor with barrier rotors,* Journal of Electrical Engineering, Vol.55, Iss.9, pp.273-276, 2004

[5] ***J. Faiz, A. M. Takbash:*** *Derating of three-phase squirrel cage induction motor under broken bar fault,* Facta Universitatis, Series Automatic Control and Robotics, Vol.12, Iss.3, pp.147-156, 2013

[6] **P. Pietrzak, M. Wolkiewicz:** *Comparison of selected methods for the stator winding condition Monitoring of a PMSM using the stator phase currents*, Energies, Vol.14, 2021, pp.1-23.

[7] **M. Mendizabal, A. McCloskey, J. Poza, S. Zarate, J. Iriondo, L. Irazu**: *Optimum Slot and Pole Design for Vibration Reduction in Permanent Magnet Synchronous Motors*, Applied Sciences, Vol.11, 2021, pp.1-17.

[8] **D-C. Popa, B. Văraticeănu, D. Fodorean, P. Minciunescu, C. Martis:** *High speed induction motor used in electrical vehicles*, Electrotehnică, Electronică Electrotehnică, (EEA), Vol.64, Iss.3, pp.5-11, 2016

[9] **B.D. Văraticeănu, P. Minciunescu, D. Fodorean:** *Mechanical design and analysis of a permanent magnet rotor used in high-speed synchronous motor*, Electrotehnică, Electronică, Automatică, Vol.62, Iss.1, pp.9-17, 2014

[10] **R. Anand, B. Gayathridev, B.K. Keshavan:** *Vertical Transportation: Effects of Harmonics of Drives by PM Machines*, Power Electronics and Drives, Vol.3(38), No.1, 2018, pp.47-53.

[11] **Končar-Mes**. Available: https://koncar-mes.hr/wp-content/uploads/2020/08/Electric-motors.pdf (29.10.2021)

Journal of Energy Technology

JET Volume 14 (2021) p.p. 47-56
Issue 3, November 2021
Type of article 1.01
www.fe.um.si/en/jet.html

LIMESTONE PURITY AS THE DECISIVE FACTOR FOR ITS CONSUMPTION IN THE FLUE GAS DESULPHURISATION PROCESS

ČISTOST APNENCA KOT ODLOČILNI FAKTOR NJEGOVE PORABE V PROCESU RAZŽVEPLJEVANJA DIMNIH PLINOV

Martin Bricl[1ℜ]

Keywords: Flue gas desulphurisation, limestone, limestone purity, limestone consumption

Abstract

The wet flue gas cleaning process in thermal power plants uses limestone reagent, which is ground and mixed with process water, before coming in contact with flue gases, in order to form a homogeneous suspension, which then absorbs the gaseous acid components in the flue gas cleaning process in thermal power plants (mainly sulphur dioxide) from the flue gas stream. The purity of the limestone has a significant effect on its consumption, as cleaner limestone enables the absorption of a larger amount of acidic components from the flue gas stream, with lower total consumption of the reagent - i.e. limestone.

Povzetek

Proces mokrega čiščenja dimnih plinov v termoenergetskih postrojenjih uporablja za reagent apnenec, ki se pred stikom z dimnimi plini zmelje in ustrezno zmeša z procesno vodo, z namenom tvorjenja homogene suspenzije, ki nato v proces čiščenja dimnih plinov v termoenergetskih objektih, absorbira plinaste kisle komponente (predvsem žveplov dioksid) iz toka dimnih plinov. Čistoča apnenca pomembno vpliva na porabo le tega, saj bolj čist apnenec omogoča absorbcijo večje količine kislih komponent iz toka dimnih plinov, pri manjši skupni porabi reagenta – torej apnenca.

ℜ Corresponding author: Dr. Martin Bricl mag. inž. str., Tel.: +386 51 210 620, E-mail address: bricl.martin@hotmail.com

1 LIMESTONE AS A REAGENT IN THE WET FLUE GAS DESULPHURISATION PROCESS

The wet flue gas desulphurisation process is an industrial process through which the acid components in the flue gas flow are removed (mainly in big coal-fired thermal power plants). The main equipment of the flue gas desulphurisation process is an absorber, in which the raw hot flue gases are washed and sprayed with the limestone suspension. The reagent for the absorption of acid components from flue gases is limestone, which is crushed and mixed with the process water in order to form a homogeneous suspension, with which the raw flue gases are sprayed. When the acid components are absorbed by the alkaline parts of the limestone suspension, oxidation air is injected into the absorber, helping to form a crystallisation process in the sump of the absorber, which forms gypsum as the by-product of the wet flue gas desulphurisation process. The limestone as the reagent for the process is usually supplied from a nearby quarry [1]. Since the chemical composition of the limestone can vary because of different geological compositions at various geographical locations, the laboratory analysis of the foreseen limestone is necessary before entering the basic and detailed design of the project. The reaction part of the reagent is determined based on the performed chemical analysis of the reagent. Those data are crucial since they dictate the overall consumption of the reagent within the flue gas desulphurisation process.

1.1 Reagent preparation for entering the process

Limestone, as the reagent for the desulphurisation process, needs to go through the delivery and preparation process before entering the cleaning process. Hereinafter are described the steps during which the limestone is handled, from delivery to storage, and supplying the chemical reaction in an absorber with freshly prepared limestone slurry. Figure 1 shows a limestone system overview.

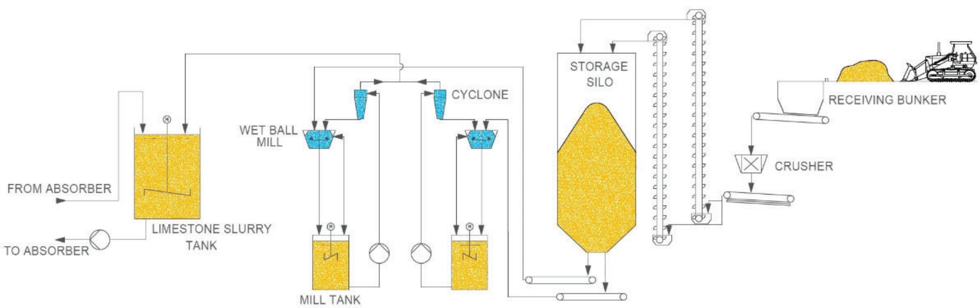

Figure 1: *Limestone receiving & storage system overview*

Handling of the limestone can be very challenging from the point of view of crushing and transporting it, since clogging of key equipment can occur [2]. Therefore, the redundancy in reagent preparation lines is meaningful. That enables the operator to operate and supply the flue gas desulphurisation process with the needed reagent through one operating reagent preparation line, while the other one is in standby just in case of clogging of the current operational line. With that model, a thermal power plant can avoid big losses in the case of an unexpected shutdown at an inconvenient operational time period.

1.1.1 Limestone delivery and unloading

As aforementioned, limestone is delivered to the site of the thermal power plant from a quarry, using trucks or trains. The standard size of the delivered limestone is usually 250 mm in diameter. This limestone is then dumped on a paved area. Where available, a covered shed is supplied for the delivered limestone, since protection from rain can prevent limestone from becoming too sticky for further manipulation with it. Dumpers are used for manipulation of the limestone from the covered shed to the receiver hopper of the crusher.

1.1.2 Limestone crushing

When the limestone is delivered to the hopper of the crusher using a dumper, the limestone pieces of 250 mm in diameter are crushed using a hammer crusher. The main task of the hammer crusher is to crush the limestone parts from 250 mm in diameter to 50 mm in diameter [3, 4]. This size enables that the limestone pieces are then transported further through the process more easily. Before the hammer crusher, a magnetic separator is installed to remove potential ferrite pieces from the handled limestone. Belt conveyors and bucket elevators are used for transporting the crushed limestone from the crusher to the storage silo facility. From the crusher, the belt conveyor is used to transport the limestone from the crusher to the bucket elevator. When the limestone enters the bucket elevator, it is elevated to the top of the silo. Additional belt conveyors can be used for further manipulation on the top of the limestone storage silo.

1.1.3 Local silo storage of crushed limestone

Crushed limestone is stored in a storage silo, which can be made out of steel or reinforced concrete. It is meaningful to design a storage silo at least for consumption of reagent of one week, or 7 working days. The limestone is stored in the limestone storage silo and, when needed, is further transported to the wet ball mill area, where it is ground finely.

1.1.4 Wet ball mill grinding and limestone slurry preparation

The limestone is transported from the storage silo to the wet ball mill area, where it enters the wet ball mill. A wet ball mill is a cylindrical mill with steel balls in it [5]. With the presence of water and rotation, the steel balls and limestone parts encounter each other, and, consequently, the limestone parts are crushed into fine particles, generally corresponding to a 325 mesh (meaning that 90% of the limestone particles are smaller than 60µm in diameter). At the outlet of the wet ball mill the limestone slurry is delivered to the hydro cyclone group, from where the underflow is delivered back to the wet ball mill, and the overflow is delivered to the freshly prepared limestone slurry storage tanks.

1.1.5 Dosing of the fresh limestone slurry to the process

Fresh limestone slurry is delivered to the absorber with the help of the limestone slurry delivery pumps, one working and one on stand-by. Freshly prepared limestone slurry is taken from the limestone slurry storage tanks and is delivered through a pipeline to the absorber. The required amount of fresh limestone slurry is then pumped into the absorber, in order to maintain a stable chemical reaction between the acid and alkali components inside the absorber. Unneeded freshly prepared limestone is returned to the limestone slurry storage tank.

2 CHEMICAL COMPOSITION OF LIMESTONE

An example of the chemical composition of the limestone [6] used as the reagent in the flue gas desulphurisation process, is presented in Table 1.

Table 1: *Example of the chemical composition of limestone*

Chemical composition of Limestone		
No.	Constituents	% by mass
1	CaO	51
2	MgO	3,8
3	Fe_2O_3	1
4	Al_2O_3	2,1
5	SiO_2	4,5
6	MnO_2	0,12
7	P_2O_5	0,01
8	Cl_2	0,015
9	Na_2O	0,16
10	K_2O	0,01
11	TiO_2	0,02
12	S	0,1
13	Bond work index	13
14	Size	250 mm

As presented in Table 1, twelve chemical elements and compounds are present in the limestone. The chemical compounds CaO and MgO represent the major part, in percentage by mass, [7]. Those two compounds are also the most important for the flue gas desulphurisation process, since they are delivering alkaline components back to the process. All the other elements do not have a significant impact on the process of flue gas cleaning itself. The initial delivered size of limestone is 250 mm in diameter before it enters the process of crushing, storing and fine wet grinding. The Bond work index [8, 9, 10] of the observed limestone sample is determined as follows.

$$W_i = 1{,}1 \cdot \frac{44{,}5}{P_c^{0{,}23} \cdot G^{0{,}82} \cdot \left(\frac{10}{\sqrt{P_{80}}} \cdot \frac{10}{\sqrt{F_{80}}}\right)} \quad (2.1)$$

$W_i - Bond\ work\ index\ \left[\frac{kWh}{t}\right]$

$P_c - Test\ sieve\ mesh\ size\ [\mu m]$

$G - Weight\ of\ the\ test\ sieve\ undersize\ per\ mill\ revolution\ [g/rev]$

$P_{80} - \ Opening\ of\ sieve\ passing\ 80\%\ of\ the\ last\ cycle\ sieve\ undersize\ product\ [\mu m]$

$F_{80} - Sieve\ mesh\ size\ passing\ 80\%\ of\ the\ feed\ before\ grinding\ [\mu m]$

3 PURITY AND REACTIVE PART OF LIMESTONE VERSUS REAGENT CONSUMPTION

The purity of limestone and its reactive part are the most important factors that have an impact on the overall consumption of limestone in the process of flue gas desulphurisation. As seen in Table 1, the calcium and magnesium content is expressed as CaO and MgO [11]. The aforementioned compounds need to be recalculated with the help of the compound molecular mass to the $CaCO_3$ and $MgCO_3$ content in % by mass. This is achieved by the following equations.

$$CaCO_3\ (\%\ by\ mass) = CaO\ (\%\ by\ mass) \cdot \frac{M\left(CaCO_3\ \frac{g}{mol}\right)}{M\left(CaO \frac{g}{mol}\right)} = CaO\ (\%\ by\ mass) \cdot \frac{100}{56} \quad (3.1)$$

$$MgCO_3\ (\%\ by\ mass) = MgO\ (\%\ by\ mass) \cdot \frac{M\left(MgCO_3\ \frac{g}{mol}\right)}{M\left(MgO \frac{g}{mol}\right)} = MgO\ (\%\ by\ mass) \cdot \frac{84{,}3}{40{,}3} \quad (3.2)$$

3.1 $CaCO_3$ Reactivity

The reactivity of $CaCO_3$ is determined based on the different requests regarding dimensioning the process equipment, as well as issuing requested guarantees. For the purpose of designing and sizing the process equipment, the reactive content of $CaCO_3$ shall be 89%, and the remaining part shall be considered unreactive, since it contains particles of impurities. For determining the guaranties, the $CaCO_3$ reactive part [12, 13, 14] in limestone shall be considered 79%, while the remaining part is unreactive with impurities. The aforementioned reactive parts are presented in Table 2 below.

Table 2: *$CaCO_3$ reactivity part for the design and guarantee scenario*

Scenario	Compound	Reactive part (% by mass)	Non-reactive part (% by mass)
Design scenario	$CaCO_3$	89	11
Guarantee scenario	$CaCO_3$	79	21

3.2 $MgCO_3$ Reactivity

The reactivity of $MgCO_3$ is determined by chemical analysis. Based on the aforementioned, the presence of $MgCO_3$ is confirmed in the limestone compound. From the limestone analysis, we can see the quantitative presence of $MgCO_3$ in limestone. In the case that the limestone`s quality is lower and it is contaminated with many impurities, the reactivity part of the $MgCO_3$ compound can be negligible. Nevertheless, if the limestone has good quality, the $MgCO_3$ presence in limestone can be also around 3 % by weight, and its reactivity up to 30%. Hence, it is important to perform several different iterations, taking into consideration different presence (by weight) and different reactivity shares.

3.3 Reagent Consumption

For the evaluation of limestone consumption, we will take into consideration a thermal power plant unit with 600MW_{th} rated capacity. The considered limestone is used for the cleaning of the flue gases within the flue gas desulphurisation process. Limestone is used as the reagent in the process. The different limestone samples shall be taken into consideration in the phase of designing. Five limestone samples with different compositions are presented in Table 2. Those five samples will be used further in the process of determining the overall limestone consumption in the flue gas desulphurisation process for the 600MW_{th} thermal power plant unit. Limestone sample number 1 has the lowest $CaCO_3$ presence and the highest amount of inert compounds and remaining impurities. Limestone sample number five has the highest $CaCO_3$ presence, with a minimal amount of inert compound and remaining impurities. The limestone samples two, three, and four have different chemical structures, where the $CaCO_3$ presence is rising from sample number two to sample number four, and impurities are decreasing. The amount of $MgCO_3$ is distributed randomly between five limestone samples, in order to see its impact on the overall reagent consumption. The reactivity level of the $CaCO_3$ compound in the limestone sample is distributed randomly between five samples, ranging from 75% - 89%. The reactivity of the $MgCO_3$ is distributed evenly between the five samples, increasing from sample number one with 10% reactivity to sample number five with 30% of reactivity. The limestone samples are presented in Table 3.

Table 3: *Example of limestone samples` chemical composition*

Limestone Sample	CaCO3 presence*	Reactivity CaCO3	MgCO3 presence*	Reactivity MgCO3	Inert compounds*	Remaining compounds*
No. 1	75	75 - 85%	2	10%	5	18
No. 2	79	75 - 85%	1	15%	4	16
No. 3	85	75 - 85%	3	20%	3	9
No. 4	89	75 - 85%	1	25%	2	8
No. 5	95	75 - 85%	1	30%	2	2
* % by the limestone sample weight						

The corresponding limestone samples are further presented graphically with the following Figure 2. Limestone sample number 1 possesses the lowest $CaCO_3$ content with the highest amount of impurities in the sample, while limestone sample number five possesses the highest amount of $CaCO_3$ in the sample and the lowest amount of impurities in the sample. Based on the proposed chemical composition of the limestone samples, we expect that sample number 1 will result in the highest reagent consumption in the flue gas desulphurisation process, while limestone sample number 5 will reflect the most optimal reagent consumption in the aforementioned process. It is important to highlight the fact that impurities that are entering the process with the reagent are blocking the chemical reactions of removing the acid components from the flow of the untreated flue gases. Therefore, it is important to supply limestone to the site as pure as possible.

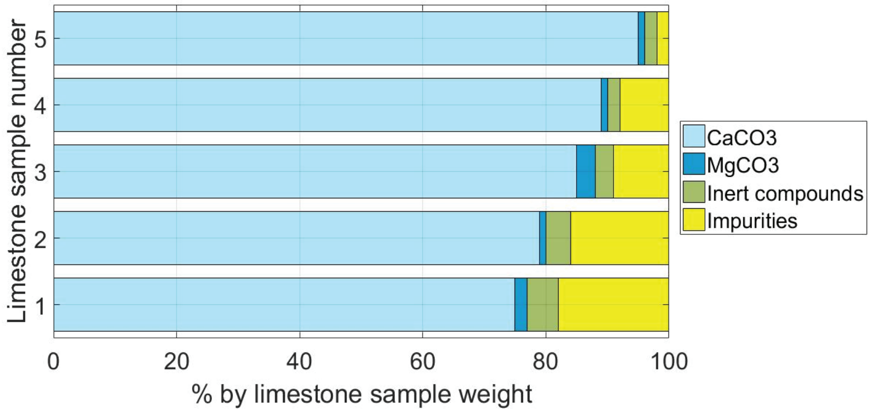

Figure 2: *Limestone samples` chemical composition*

Based on the chemical composition of five limestone samples, we calculated the expected overall limestone consumption of the flue gas desulphurisation process. As predicted previously, limestone sample 1 reflects the highest limestone consumption with only 75% $CaCO_3$ presence in the sample, and with the overall consumption of 10855 kg/h, taking into consideration that the sample has a 75% $CaCO_3$ reactivity part.

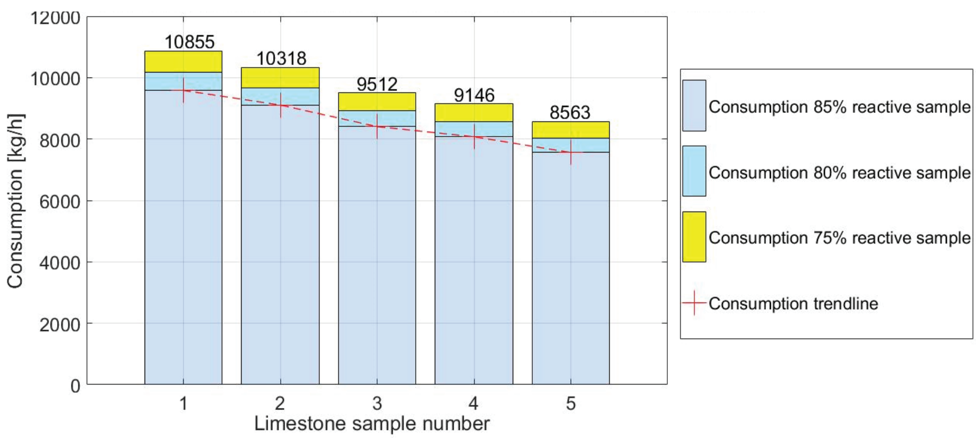

Figure 3: *Limestone samples one to five and their overall consumption in kg/h in the flue gas desulphurisation process*

Contrary to limestone sample one, limestone sample five possesses 95% $CaCO_3$ presence, and with the reaction part 75% of it, we can expect 8563 kg/h limestone consumption. The correlation between the purity of the reagent limestone and its consumption we are presenting in the following Table 4. The difference between the consumption of different reagent reactivity samples is presented in the last two columns of Table 4. Based on the calculated and presented data, we can conclude that the correlation between the purity of the limestone sample and its consumption is inversely proportional. It is to be expected that the purest limestone will result in lower consumption, and vice versa. In Table 4, column number 5, the difference in overall limestone consumption is presented, between samples with a 75% reactivity part and 80% reactivity part samples. It is shown in column number 5 that this difference is approximately half of the tonne of the limestone reagent consumption per hour (12 tons of reagent limestone savings per operating day of the flue gas desulphurisation system). Furthermore, in Table 4, column number 6, the difference is presented in overall consumption between samples with 75% reactivity part and an 85% reactivity part. From the data in Table 4, column number 6, we can see that the limestone consumption savings are around 1 ton of the limestone reagent per operating hour of the flue gas desulphurisation system (24 tons of reagent limestone savings per operating day of the flue gas desulphurisation system). From the consumption analysis presented in Table 4, it is clear that it is in the highest interest of the thermal power plant owner or operator that the purest limestone is delivered to the site, with the highest reactivity part possible. This kind of limestone will allow smooth flue gas desulphurisation plant operation, without any unnecessary clogging, as well as lowering the operating and maintenance costs of the flue gas desulphurisation system.

Table 4: *Limestone reagent samples 1 to 5 overall consumption in the FGD process*

Limestone Sample No.	① 75% Reaction Sample Consumption [kg/h]	② 80% Reaction Sample Consumption [kg/h]	③ 85% Reaction Sample Consumption [kg/h]	Δ ① - ② [kg]		Δ ① - ③ [kg]	
Sample 1	10855	10180	9583	675	Savings of the limestone reagent 6,2%	1272	Savings of the limestone reagent 11,7%
Sample 2	10318	9675	9107	643		1211	
Sample 3	9512	8924	8404	588		1108	
Sample 4	9146	8576	8074	570		1072	
Sample 5	8563	8031	7560	532		1003	

4 CONCLUSION

This paper presents the main effect of limestone purity (and its reactivity) on the overall consumption of the limestone as a reagent in the flue gas desulphurisation process. Five limestone samples with different purity rates, as well as different reactivity rates, are presented in the paper. A $600MW_{th}$ thermal power plant FGD unit is considered for the purpose of the reagent consumption simulation. It is concluded that the limestone sample with the highest purity and reactivity is resulting in the lowest regent consumption. Therefore, it is highlighted in the concluding phase of this paper, that FGD unit operators (owners) should strive to supply as good a reagent as possible to their operating or planned FGD units, in order to establish a continuous and reliable chemical reaction that will remove a sufficient grade of the acid components in the raw flue gas flow from the thermal power plant boiler. Consequently, operating FGD costs will also be lower.

References

[1] **J.A.H. Oates**: *Lime and Limestone Chemistry and Technology Production and Uses*, Wiley VCH Verlag GmbH, p.p. 169, 1998

[2] **M. Kepniak, P. Woyciechowski, W. Franus**: *Chemical and physical properties of limestone powder as a potential microfiller of polymer composites*, Archives of Civil Engineering, Vol. LXIII, Issue 2, p.p. 67 – 78, 2017

[3] **Ö. Kilic**: *Impact of physical properties and chemical composition of limestone on decomposition activation energy*, Asian Journal of Chemistry, Vol. 25, p.p. 8116 – 8120, 2013

[4] **M.I. Smorodinov, E.A. Motovilov, V.A. Volkov**: *Determination of Correlation Relationship Between Strength and Some Physical Characteristics of Rocks*, Proceedings of the of the Second Congress of the International Society of Rock Mechanics, Vol. 2, p.p. 35, 1970

[5] **L.M. Tavares, R.D.C. Kallemback**: *Grindability of Binary Ore Blends in Ball Mills*, Minerals Engineering, Vol. 41, p.p. 115 – 120, 2013

[6] **P. Šiler, I. Kolarova, J. Bednarek, M. Janča, P. Musli, T. Opravil**: *The possibilities of analysis of limestone chemical composition*, International conference building materials, product and technologies, Vol. 379, p.p. 1 – 6, 2018

[7] **F. Munawaroh, L. Khamsatul Muharrami, T. dan Zaenal Arifin**: *Calcium oxide characteristics prepared from Ambuten's calcined limestone*, Jurnal Pena Sains, Vol. 5, No. 1, p.p. 65 – 71, 2018

[8] **D. Todorović, Z. Bartulović, V. Jovanović, B. Ivošević**: *The bond work index of limestone and andesite mixtures*, Mining and metallurgy BOR, No. 3 – 4, p.p. 21 – 28, 2017

[9] **H. Ipek, Y. Ucbas, C. Hosten**: *The Bond Work Index of Mixtures of Ceramic Raw Materials*, Minerals Engineering, Vol. 18, p.p. 981 – 983, 2005

[10] **P.C. Kapur, D.W. Fuerstenau**: *Simulation of Locked-Cycle Grinding Test Using Multicomponent Feeds*, Powder technology, Vol. 58, p.p. 39 – 48, 1989

[11] **Y. Zhu, S. Wu, X. Wang**: *Nano CaO grain characteristics and growth model under calcination*, Chemical Engineering Journal, Vol. 175, p.p. 512 – 551, 2011

[12] **Z. Arifin, N. F. Apriliani, M. Zainuri, M. Darminto**: *Characterization of Precipitated $CaCO_3$ Synthesized from Dolomite*, IOP Conference Series Material Science and Engineering, Vol. 196, p.p. 1 – 4, 2017

[13] **M.V. Kök, W. Smykatz-Kloss**: *Characterization, Correlation and Kinetics of Dolomite sample as outlined by Thermal Methods*, Journal of Thermal Analysis and Calorimetry, Vol. 91, No. 2, p.p. 565 – 568, 2008

[14] **N.L. Ross, R.J. Reeder**: *High pressure structural study of dolomite and ankerite*, American Mineralogist, Vol. 77, p.p. 412 – 421, 1992

Nomenclature

(Symbols)	(Symbol meaning)
mm	millimetres
µm	micrometres
FGD	Flue gas desulphurisation
CaO	Calcium oxide
MgO	Magnesium oxide
Fe_2O_3	Iron (III) oxide (ferric oxide)
Al_2O_3	Aluminium (II) oxide
SiO_2	Silicon dioxide
MnO_2	Manganese dioxide
P_2O_5	Phosphorus pentoxide
Cl_2	chlorine
Na_2O	Sodium oxide
K_2O	Potassium oxide
TiO_2	Titanium dioxide
S	sulphur
$CaCO_3$	Calcium carbonate
$MgCO_3$	Magnesium carbonate
MW	megawatt
th	thermal
kg	Kilogram
kg/h	Kilograms per hour

Journal of Energy Technology

JET Volume 14 (2021) p.p. 57-72
Issue 3, November 2021
Type of article 1.01
www.fe.um.si/en/jet.html

MEASUREMENTS OF THE CHARACTERISTICS OF AN ELECTRIC MOTOR FOR AN ELECTRIC VEHICLE`S DRIVE

MERITVE KARAKTERISTIK ELEKTROMOTORJA ZA POGON ELEKTRIČNEGA VOZILA

Klemen Srpčič[1ℜ], Gregor Srpčič[1]

Keywords: electric vehicles, electric motor, brushless DC motor, solar-powered vehicle

Abstract

This paper aims to present the performance and measurement results of a load test performed on a brushless DC motor built into the wheel of a solar-powered vehicle. A brushless DC motor's theoretical background and operation are presented at the beginning of the paper. The article covers the technical specification of the solar-powered vehicle and the inbuilt brushless DC motor. The measurements were performed with the described equipment at the Institute of Energy Technology, Faculty of Energy Technology, University of Maribor. Due to the unique design of the measured electric motor, it was also necessary to make a special housing, which was intended for connecting the electric motor to the test bench. The article concludes with an analysis of the measurement results in comparison with the data provided by the electric motor manufacturer.

Povzetek

Cilj prispevka je predstaviti izvedbo in rezultate meritve obremenitvenega testa enosmernega brezkrtačnega motorja, ki je vgrajen v kolo solarnega vozila. V začetku prispevka je najprej predstavljeno

ℜ Corresponding author: Klemen Srpčič, B.Sc., E-mail address: klemen.srpcic@student.um.si

[1] University of Maribor, Faculty of Energy Technology, Hočevarjev trg 1, 8270 Krško, Slovenia

teoretično ozadje zgradbe in delovanja enosmernega brezkrtačnega motorja. Prispevek zajema tehnične specifikacije solarnega vozila in vgrajenega električnega motorja. Meritve so bile opravljene s predstavljeno opremo na Inštitutu za energetiko, Fakultete za energetiko Univerze v Mariboru. Zaradi posebne izvedbe merjenega motorja je bilo potrebno izdelati tudi posebno ohišje, ki je namenjeno priklopu motorja na merilno mesto. V zaključku je podana tudi analiza rezultatov meritev v primerjavi s podatki, ki so bili podani s strani proizvajalca motorja.

1 INTRODUCTION

Electric vehicles are an old idea, which has become more and more popular in recent times, since they embody our green-oriented mentality. Their development started more than a century ago in France and England, which were the first countries that started developing electric propulsion systems. Since then, electric cars have gone through their ups and downs. They had some advantages over petrol cars, such as, they were quieter, did not spread a stench, they were not causing vibrations when functioning and there was no need to shift gears. However, in the 1920s electric vehicles lost their dominance over internal combustion engine vehicles. The main reasons were the construction of long roads between cities that required a longer reach of vehicles and the reduction of the oil price, which reduced the cost of the use of vehicles with internal combustion engines. [1-3]

Since then, electric vehicles have been used mainly for specific purposes, such as small transport vehicles with short-range, golf carts, etc. However, the oil crisis in the seventies has awakened the interest in electric vehicles, and environmental agencies instructed car manufacturers to invest in the development of vehicles with low emission levels. Therefore, the main objective was to develop electric vehicles with zero emissions. [1], [4]

The most significant breakthrough was the EV1 model produced by General Motors, which represented the only car that met all the objectives of the Office for Energy of the United States of America. It was offered to customers through a Lease Agreement between 1996 and 2002. Since then, many car companies have started developing different types of electric cars, namely, plug-in hybrids, extended-range electric vehicles, battery electric vehicles and solar-powered electric vehicles. [1], [4]

A solar-powered electric vehicle was also developed by high school students and their teachers in the Krško-Sevnica School Centre. This School Centre participates in custom-made solar-powered electric vehicle races actively and successfully. The Faculty of Energy Technology and Krško-Sevnica School Centre implemented a common project founded by the Student innovative projects for social benefit (ŠIPK) programme. The project's main goal was the measurement of the load characteristics of the electric brushless DC motor (BLDC), which will also be the main topic of this article. Based on the performed measurements, data were obtained on the performance characteristics of the BLDC motor, which will make it possible to optimise the performance of the solar-powered car further. In addition, the project described the theoretical foundations of electric motors, control of electric drives, and the legislation related to electric mobility, which will provide the students of Krško-Sevnica with materials to help them continue their work on the solar-powered car.

As already mentioned, this article will focus on the BLDC motor of the solar-powered car and the measurement of its load characteristics. The BLDC motor and the custom-made solar-powered vehicle will be described in Chapters 2 and 3. Chapter 4 will present the test site and measurement system, including the measurement devices at the Institute of Energy Technology in the Laboratory for Electric Machines and Drives. The load characteristic measurements and measurement results will be shown in the last Chapter.

2 ELECTRIC MOTOR

An electric motor is a device that converts electric energy into mechanical energy. They are divided into DC and AC motors in the most general aspect. This is a basic distribution, based on the supply voltage source fed to the electric motor. Other electric motors can be divided into subcategories. Under AC motors, we understand the terms induction and synchronous motors. The latter can be divided further into permanent magnet motors, stepper motors, reluctance motors, etc. Under the category DC motors there are roughly two main groups, namely, brushed and brushless DC motors. [5]

A rough distribution of the types of electric motors is shown in Figure 1.

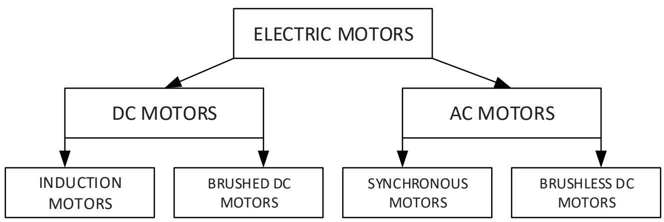

Figure 1: *Rough distribution of electric motors into categories*

2.1 Brushless DC motor (BLDC)

BLDC motors are used widely in electric vehicle drives as in-wheel motors. As the name suggests, in-wheel motors are built into the wheel of a vehicle, which improves the whole system's efficiency. Among the most important features of BLDC motors are low torque ripple, high efficiency, reliable operation and long life span. Due to the absence of brushes, there is no sparking during their operation, so they can also be used in hazardous areas. The positive properties of this type of electric motor can meet the needs of various applications. BLDC motors are used in robotics, household appliances, computer equipment and the automotive industry. [5], [6]

BLDC motors are similar to synchronous motors, with permanent magnets in their structure. However, their operation is similar to that of a brushed DC motor. From the basic version, they differ mainly in the magnetic field distribution. Due to its structure, this type of motor has a lower mass and moment of inertia, which, in practice, means better dynamics as a response to control signals. Compared to the brushed DC motor this type is better, even when it comes to efficiency, size and maintenance, as it does not need brushes for its operation. Brushes tend to wear down and require replacement for the motor to function properly. There are two basic versions of a BLDC motor. In the first, the stator is connected to the motor housing, and in the second, the motor housing is a rotor. We call the first version an "inrunner" and the second an "outrunner" motor. [5-8]

The stator core of a BLDC is made of steel, and is laminated to reduce the occurrence of eddy currents. Stators have different variations of stator winding grooves that can also be skewed. In addition to stators with grooves, there are also stator designs without grooves. We need a larger air gap between the rotor and the stator when using such stators. This, consequently, reduces the field of magnetic excitation of the permanent magnet. The problem can be solved by increasing the height of the permanent magnets, which also increases the motor's price. Such designs are used mainly when we need high speeds and performances. [5]

The rotor of BLDC motors is made of low carbon solid steel or of the same material as the stator. The magnets can be surface mounted on the rotor or located inside the rotor. Materials such as aluminium-nickel-cobalt, samarium-cobalt, and neodymium-iron-boron are used most commonly for magnets. Neodymium magnets currently allow the highest magnetic energies to be achieved, but have problems with temperature stability. Another downside is their price, which is also slightly higher compared to the price of ferrite magnets. [5], [7]

Instead of a commutator and brushes, BLDC motors use a controller or an electronic converter circuit connected to the stator winding. The electronic converter circuit detects the motor's position due to the built-in Hall sensors. Based on the rotor position information, it switches the current on and off through the appropriate windings on the stator. The rotational speed of the motor depends on the switching frequency of the switching device. Electronically commutating machines typically have three or more windings. [5], [8]

Figure 2 presents a simple cross-section view of a BLDC motor.

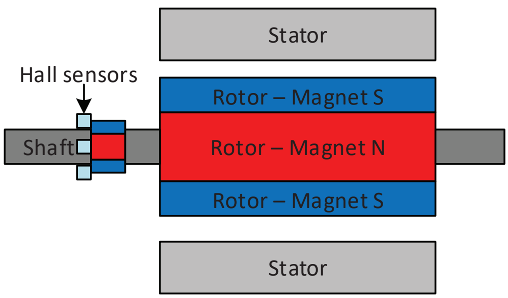

Figure 2: *A simple cross-section view of a BLDC motor*

3 ELECTRIC SOLAR-POWERED VEHICLE

The custom-made solar-powered vehicle shown in Figure 3 is a product of the students and teachers from the Krško-Sevnica School Centre. It was made with the goal to participate in a race of solar-powered electric vehicles in the city of Sisak. The vehicle was designed to meet all the required characteristics prescribed for the race. The project involved students of Mechanical and Electrical Engineering the high school, who constructed a solar-powered car with their mentors. When manufacturing, it was necessary to consider that the power of the motors should not exceed 1500 W, the minimum area of solar cells should be 3 m^2, and the mass of batteries should not be less than 80 kg. The vehicle must also be equipped with brakes on all wheels.

The technical data of the solar vehicle are given in Table 1.

Figure 3: *Custom made solar-powered electric vehicle*

Table 1: *Technical data of the solar-powered electric vehicle*

Length	2,85 m	
Width	1,75 m	
Height	1,4 m	
Total mass	260 kg	
Mass of batteries	84 kg	
Motor type	BLDC 1500 W / 48 V	
Solar modules	Type	PERLIGHT PLM-020M-36
	Module area	3,5 m^2
	Number of modules	20
	Current	1,13 A
	Voltage	17,3 V
	Power	20 W
Battery type	55 AGM 12 V / 70Ah	
Construction material	Aluminium	
Brakes	HYDRAULIC BRAKES	
Additional equipment	Speedometer and LED speed display Control and display of driving direction Battery voltage control Charging control Rear view camera Driving recording Display of controller, ambient and module temperatures	

All the wheels of the solar-powered electric vehicle have an in-built BDLC Hub Motor type QSMOTOR 205 V2 with a rated power of 1500 W and a rated voltage of 48 V. The considered motor is shown in Figure 4, and detailed motor specifications are given in Table 2.

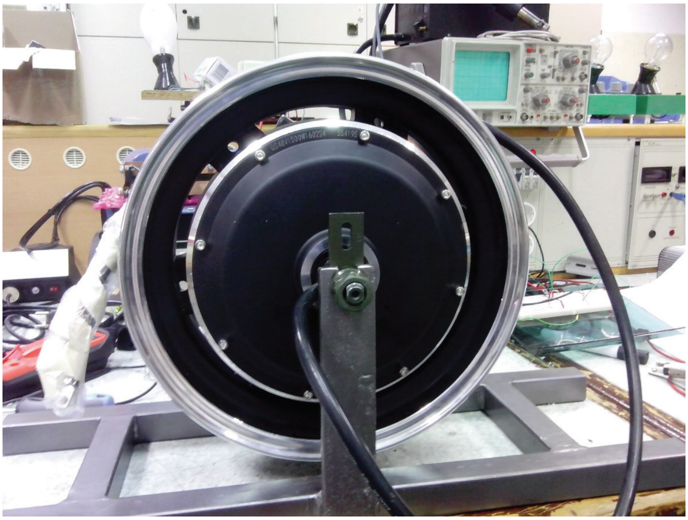

Figure 4: *BDLC Hub Motor type QSMOTOR 205 V2*

Table 2: *BDLC Hub Motor type QSMOTOR 205 V2 specifications*

Motor dimensions	**Motor diameter**	332 mm
	Wheel size	30,48 x 8,89 cm
	Wheel material	Aluminium
	Tyre	120/70-12, 90/90-12
Motor data	**Number of phases**	3
	Cable cross-section	8 mm^2
	Rated power	1500 W
	Max power	2000 W
	Rated voltage	48 V
	Rated current	31 A
	Max current	47 A
	Max torque	110 Nm
	Efficiency	89 %
	Rotational speed	400-690 rpm
	Top speed	55 km/h
	Protection level	IP54
	Max permitted temperature	70 °C
	Colour	Black

4 MEASUREMENTS

The measurements of the aforementioned motor were performed at the Institute of Energy Technology in Vrbina, Krško, in the Laboratory for Electrical Machines and Drives. The test site and the used measurement equipment will be described in the following subchapters. Also presented will be the motor mounting process and load test protocol .

4.1 Test site

In the Laboratory for Applied Electrical Engineering (LAE) and the Laboratory for Electrical Machines and Drives (LESP) at the Institute of Energy Technology, in addition to other activities, measurements of electrical machines are also performed as part of the research work. The basis for performing the measurements of electric motors are three test benches (Figure 5). All three test benches are 3D adjustable, and all have active brakes that are water-cooled. They also enable water cooling of the tested electric machine, if necessary. The largest of the benches also has a hydraulic lift with a capacity of up to 1000 kg, which allows movement and adjustment of the subjects of even larger dimensions or masses.

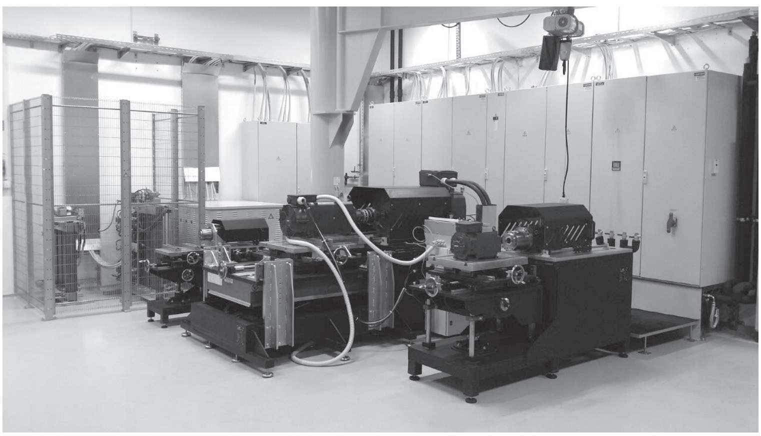

Figure 5: *Test site at the Institute of Energy Technology*

The measurements were performed on the middle-sized test bench, which allows measurements up to a power of 72 kW and a rotational speed of up to 15,000 rpm. The test bench enables the measurement of tested electrical machines with axial heights from 160 mm to 380 mm. An active brake is a synchronous machine with permanent magnets. This test bench was chosen mainly because of the appropriate axial height of the tested BLDC motor.

In order to connect the solar-powered vehicle drive to the active brake, it was necessary to construct a special mount due to the design of the measured BLDC motor. The construction of the attachment will be presented in the following subsection. The BLDC motor is connected to the active brake via a Lorenz DR-2643 speed and torque sensor (Figure 6), which enables speed measurements of up to 15,000 rpm and torque measurements of up to 100 Nm. The measured motor and active brake must be centred precisely to avoid unnecessary vibrations transmitted to the speed and torque sensor, and thus affect the measurement accuracy. A Prüftechnik Optalign Smart Ex centring device (Figure 7), which enables laser position adjustment, was used to align the subject under test and the active brake accurately.

Figure 6: *Lorenz DR-2643 speed and torque sensor*

Figure 7: *Prüftechnik Optalign Smart Ex cantring device*

The measured mechanical and electrical quantities were captured with a Yokogawa WT 1806 (Figure 8) power analyser, which is a reliable, high-performance analyser. It has the option to measure electrical quantities on six input channels, and ensures a measurement accuracy of 0,05 %. The power analyser was connected to a computer via the WT Viewer measurement program. The program is intended for managing power analyser settings, and capturing and analysing all measured data from the analyser. The program also allows data to be stored in .dat format, so the measured data were analysed in the Matlab software environment. [9]

Figure 8: *Power analyser Yokogawa WT1806*

A SCADA system (Figure 9), which was used for control of the power supply of the tested machine, cooling, operation of the external power plant, and active brakes, was used to control the active brake. When controlling individual test benches, it also allows us to set the speed and torque limit to prevent damage to the measurement equipment or electric motors in case of human error.

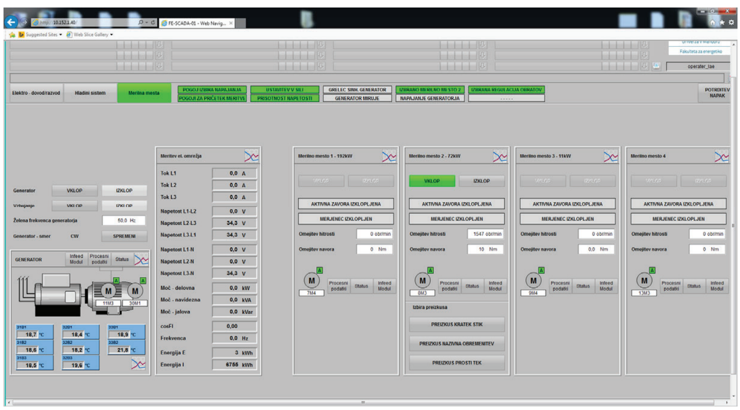

Figure 9: *SCADA system*

4.2 Electric motor mounting

The test benches in LAE and LESP are intended for testing of standard electric motor designs. In this case, the measurements had to be performed on a BLDC motor built into the wheel of a solar-powered vehicle. For this reason, it was necessary to make a housing to mount the electric motor which clamps to the test bench and keeps the electric motor in balance and prevents rotational movement of the wheel. It was also necessary to construct a part supported by bearings, which was intended to be connected to the shaft of the active brake. 3D models of individual components of the BLDC motor mount, drawn with the software package SolidWorks, are presented below.

The mount is made from one piece. There are two holes in the housing; the smaller hole is intended for rigid mounting of the electric motor, and the bearing part will be supported on the larger one. There is also a circlip in the larger hole to prevent axial movement. Figures 10 and Figure 11 show the isometric view and cross-section of the motor mount model.

The bearing part, which rotates together with the electric motor, is intended for connection to the active brake shaft. It is attached to the electric motor using three screws. The cross-section also shows the indentation in which the shaft of the electric motor is installed. There is also a dowel groove on the shaft to prevent the clutch from slipping. Figures 12 and 13 show the isometric view and cross-section of the bearing model.

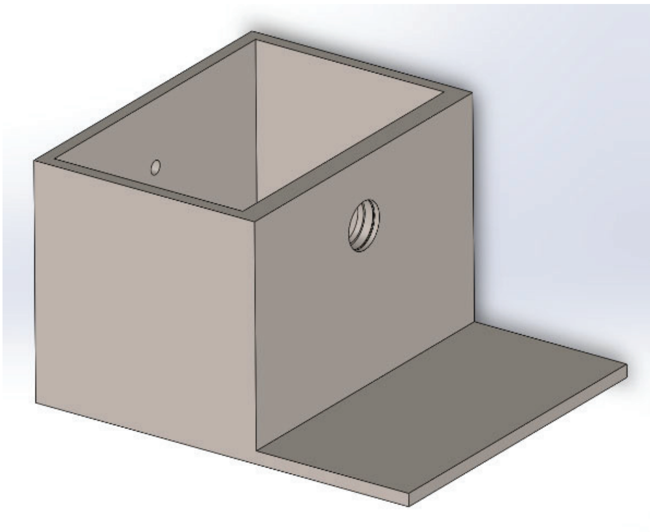

Figure 10: *Isometric view of the motor mount model*

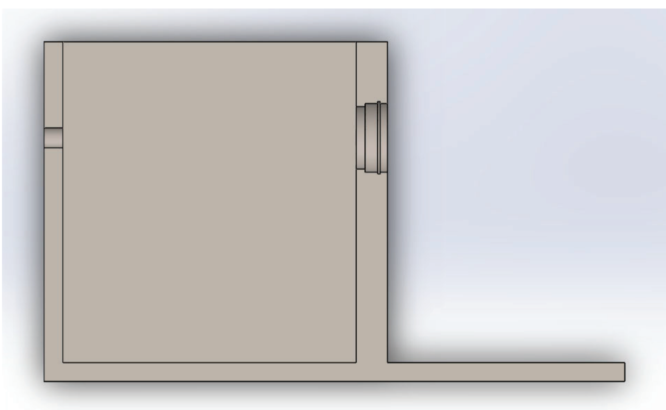

Figure 11: *Cross-section of the motor mount model*

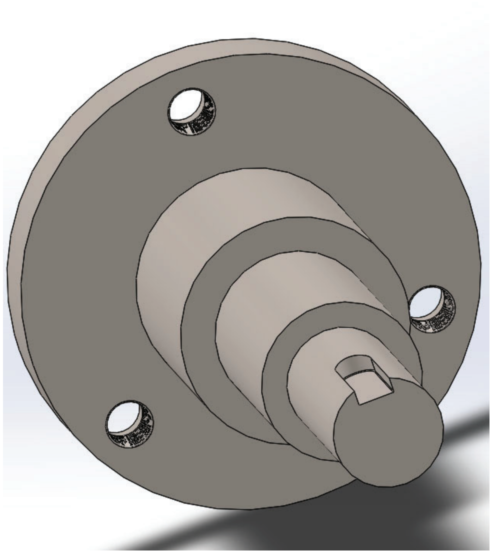

Figure 12: *Isometric view of the bearing part*

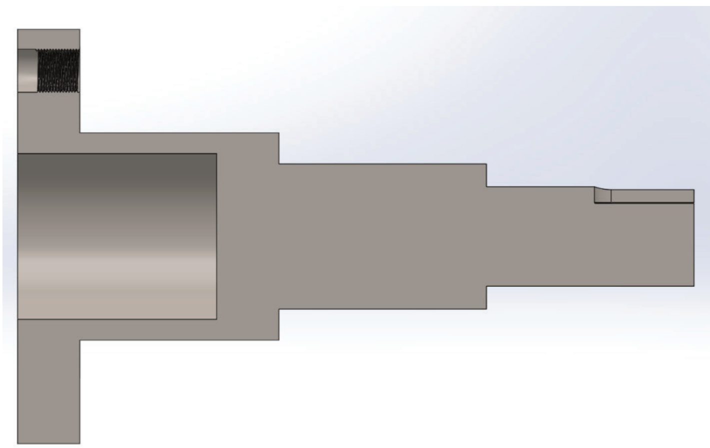

Figure 13: *Cross-section of the bearing part*

Figure 14 shows the common assembly of the constructed motor mount and the tested BLDC motor.

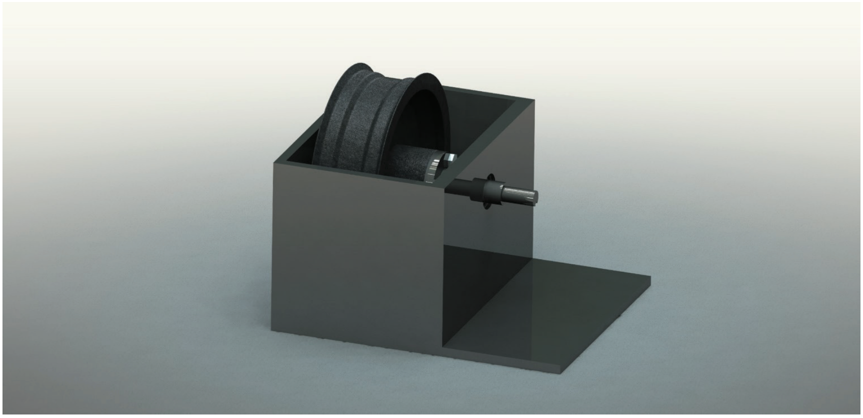

Figure 14: *Assembly of the motor mount and BLDC motor*

4.3 Load test measurement

The load measurement of the tested BLDC motor is performed by supplying the motor with a nominal voltage of 48 V via the controller and starting to load it. The BLDC motor is loaded by increasing the torque of the active brake, which acts as a load on the measured motor. The active brake is controlled via the SCADA system. All electrical quantities were measured with the Yokogawa WT1806 power analyser, and mechanical quantities were measured with a Lorenz DR-2643 torque and speed sensor. All the measured quantities were captured with the Yokogawa WT1806 and transferred to a PC for further processing.

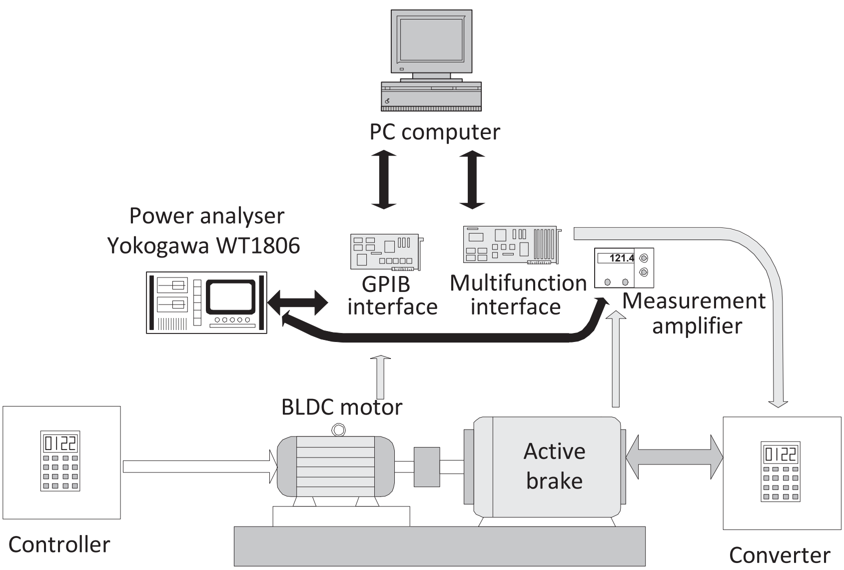

Figure 15: *Schematic of the test site at the Institute of Energy Technology*

5 RESULTS

The torque was increased incrementally during the measurement. As the torque (*M*) increased, the electric current (*I*) also began to increase, and the rotational speed (*n*) began to decrease, as can be seen from the plotted graph in Figure 16. Electric voltage (*U*) was constant throughout the measurement and had a value of 48 V. From the chart in Figure 15, we can see that, as the electric current increases the input electric power (P_{in}) also increases, and the losses in the windings also increase, growing with the square of the current. When the torque is below approximately 35 Nm, it can be seen that, despite the decrease in rotational speed, the mechanical power increases, which, later, begins to decrease when the rotational speed drops sharply. Finally, the efficiency curve reaches a maximum value at 84,3%.

The data obtained with the load measurements were compared with the data provided by the manufacturer of the BLDC motor. During the comparison, quite a few discrepancies were noted between the measured and manufacturer`s data. The manufacturer states a maximum torque of 110 Nm, which we did not meet with the measured values. At 87 Nm, the measurement was finished, as the maximum current specified by the manufacturer had already been exceeded by 10 A.

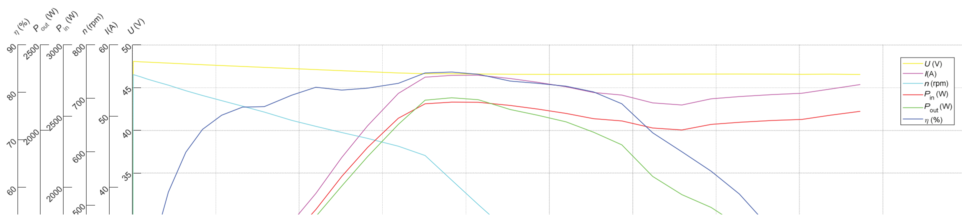

Nomenclature

(Symbols)	(Symbol meaning)
A	the area of the outer envelope of a building
a_H	dimensionless parameter
A_u	usable area of building
A_{window}	window area
B_h	direct solar irradiation on horizontal surface
d	layer thickness of the building structure
D_h	diffuse solar irradiation on horizontal surface
d_w	the number of days of hot water supply in a given period
E_{HP}	required electricity for the operation of the heat pump
F_c	blinds factor
F_f	frame factor

measured efficiency was 84,3 %. Thus, the maximum mechanical power given by the manufacturer (2000 W) was exceeded. Still, the efficiency given by the manufacturer (89 %) was not reached. The rotational speed was in the range specified by the manufacturer. The most significant deviation is shown in the electric current value, as it can be seen that the measured values greatly exceeded the nominal value of the electric current.

Table 3: *Measurement results and manufacturer's data*

	Measured values at nominal output power	**Measured values at maximum efficiency**	**Manufacturer`s data**
Torque *M* [Nm]	22	38,3	/
Voltage *U* [V]	47,12	46,63	48
Current *I* [A]	39,14	55,72	31
Rotational speed *n* [rpm]	647,5	546,6	400 – 690
Electric power P_{in} [W]	1844	2598	/
Mechanical power P_{out} [W]	1496	2191	1500
Efficiency [%]	81,1	84,3	89

6 CONCLUSION

Due to their properties, BLDC motors are used most commonly in applications for electric vehicles. The custom-made solar-powered vehicle also has the aforementioned type of electric motor, which is built into the wheel of the vehicle. Because of the in-wheel build of the BLDC motor, a special housing was made for the purpose of mounting the electric motor to the test bench. It was necessary that the housing kept the electric motor in balance and prevented the wheel's rotational movement.

The load measurement of the tested BLDC motor was performed by supplying the motor with a nominal voltage of 48 V, and the torque was increased incrementally during the measurement. The aim was to compare the results of the measurements with the data provided by the manufacturer of the BLDC motor. The comparison indicated quite a few differences between the two sets of data. More measurements would be needed for a more accurate analysis of the results and the given technical specifications of the BLDC motor. Nevertheless, the obtained data on the performance characteristics of the electric motor were helpful for optimising the performance of the solar-powered vehicle.

References

[1] **L. Juteršek:** *Smiselnost nakupa električnega avtomobila*, Fakulteta za logistiko, Univerza v Mariboru, 2012. Available: https://dk.um.si/Dokument.php?id=51626 (5. 12. 2021)

[2] **M. Bellis:** *The history of electric vehicles began in 1830 [Online]*, Available: https://www.thoughtco.com/history-of-electric-vehicles-1991603 (5. 12. 2021)

[3] **J. Aleksič:** *Kratka zgodovina električnega vozila [Online]*, Available: https://www.mladina.si/45593/kratka_zgodovina_elektricnega_avtomobila (5. 12. 2021)

[4] *Electric Vehicles History Part V [Online],* Available: https://www.electricvehiclesnews.com/History/historyV.htm (5. 12. 2021)

[5] **A. Čufar:** *Poučevanje vsebin o delovanju brezkrtačnih enosmernih elektromotorjev,* Pedagoška fakulteta, Fakulteta za matematiko in fiziko, Univerza v Ljubljani, 2013. Available: http://pefprints.pef.uni-lj.si/1625/1/%C4%8Cufar_Aleksandra_DD_PDF.pdf (5. 12. 2021)

[6] **L. Urbanc**: *Model brezkrtačnega motorja za aplikacije v električnih kolesih*, Fakulteta za elektrotehniko, računalništvo in informatiko, Univerza v Mariboru, 2016. Available: https://dk.um.si/Dokument.php?id=98017 (5. 12. 2021)

[7] **M. Flis:** *Brezkrtačni motorji za električna kolesa,* Fakulteta za energetiko, Univerza v Mariboru, 2014. Available: https://dk.um.si/Dokument.php?id=69135 (5. 12. 2021)

[8] **M. Gabrijelčič:** *Razvoj perifernih vmesnikov za mobilnega robota*, Fakulteta za elektrotehniko, računalništvo in informatiko, Fakulteta za strojništvo, Univerza v Mariboru, 2016. Available: https://dk.um.si/Dokument.php?id=104841 (5. 12. 2021)

[9] **Yokogawa:** *Precision Power Analyzer, User's manual,* 2017. Available: https://cdn.tmi.yokogawa.com/IMWT1801E-01EN.pdf (5. 12. 2021)

Nomenclature

(Symbols)	(Symbol meaning)
A	ampere
Ah	ampere-hour
AC	alternating current
BLDC motor	brushless direct current motor
cm	centimetre
°C	degrees Celsius
DC	direct current
I	electric current
kg	kilogram

km/h	kilometres per hour
kW	kilowatt
m	metre
m^2	square metre
mm	millimetre
mm^2	square millimetre
M	torque
Nm	newton metre
n	rotational speed
P_{in}	input electric power
P_{out}	output mechanical power
rpm	revolutions per minute
U	voltage
V	volt
W	watt

MAIN TITLE OF THE PAPER SLOVENIAN TITLE

Author[1], Author [2], Corresponding author[ℜ]

Keywords: (Up to 10 keywords)

Abstract

Abstract should be up to 500 words long, with no pictures, photos, equations, tables, only text.

Povzetek

(Abstract in Slovenian language)

Submission of Manuscripts: All manuscripts must be submitted in English by e-mail to the editorial office at jet@um.si to ensure fast processing. Instructions for authors are also available online at http://www.fe.um.si/en/jet/author-instructions.html.

Preparation of manuscripts: Manuscripts must be typed in English in prescribed journal form (MS Word editor). A MS Word template is available at the Journal Home page.

A title page consists of the main title in the English and Slovenian language; the author(s) name(s) as well as the address, affiliation, E-mail address, telephone and fax numbers of author(s). Corresponding author must be indicated.

Main title: should be centred and written with capital letters (ARIAL bold 18 pt), in first paragraph in English language, in second paragraph in Slovenian language.

Key words: A list of 3 up to 6 key words is essential for indexing purposes. (CALIBRI 10pt)

Abstract: Abstract should be up to 500 words long, with no pictures, photos, equations, tables, - text only.

Povzetek: - Abstract in Slovenian language.

Main text should be structured logically in chapters, sections and sub-sections. Type of letters is Calibri, 10pt, full justified.

ℜ Corresponding author: Title, Name and Surname, Organisation, Department, Address, Tel.: +XXX x xxx xxx, E-mail address: x.x@xxx.xx

[1] Organisation, Department, Address

[2] Organisation, Department, Address

Units and abbreviations: Required are SI units. Abbreviations must be given in text when first mentioned.

Proofreading: The proof will be send by e-mail to the corresponding author in MS Word's Track changes function. Corresponding author is required to make their proof corrections with accepting or rejecting the tracked changes in document and answer all open comments of proof reader. The corresponding author is responsible to introduce corrections of data in the paper. The Editors are not responsible for damage or loss of submitted text. Contributors are advised to keep copies of their texts, illustrations and all other materials.

The statements, opinions and data contained in this publication are solely those of the individual authors and not of the publisher and the Editors. Neither the publisher nor the Editors can accept any legal responsibility for errors that could appear during the process.

Copyright: Submissions of a publication article implies transfer of the copyright from the author(s) to the publisher upon acceptance of the paper. Accepted papers become the permanent property of "Journal of Energy Technology". All articles published in this journal are protected by copyright, which covers the exclusive rights to reproduce and distribute the article as well as all translation rights. No material can be published without written permission of the publisher.

Chapter examples:

1 MAIN CHAPTER

(Arial bold, 12pt, after paragraph 6pt space)

1.1 Section

(Arial bold, 11pt, after paragraph 6pt space)

1.1.1 Sub-section

(Arial bold, 10pt, after paragraph 6pt space)

Example of Equation (lined 2 cm from left margin, equation number in normal brackets (section. equation number), lined right margin, paragraph space 6pt before in after line):

Equation (1.1)

Tables should have a legend that includes the title of the table at the top of the table. Each table should be cited in the text.

Table legend example:

Table 1: *Name of the table (centred, on top of the table)*

Figures and images should be labelled sequentially numbered (Arabic numbers) and cited in the text – Fig.1 or Figure 1. The legend should be below the image, picture, photo or drawing.

Figure legend example:

Figure 1: *Name of the figure (centred, on bottom of figure, photo, or drawing)*

References

[1] **N. Surname:** *Title,* Journal Title, Vol., Iss., p.p., Year of Publication

[2] **N. Surname:** *Title,* Publisher, Year of Publication

[3] **N. Surname:** *Title* [online], Publisher or Journal Title, Vol., Iss., p.p., Year of Publication. Available: website (date accessed)

Examples:

[1] **J. Usenik**: *Mathematical model of the power supply system control*, Journal of Energy Technology, Vol. 2, Iss. 3, p.p. 29 – 46, 2009

[2] **J. J. DiStefano, A.R. Stubberud, I. J. Williams**: *Theory and Problems of Feedback and Control Systems*, McGraw-Hill Book Company, 1987

[3] **T. Žagar, L. Kegel:** *Preparation of National programme for SF and RW management taking into account the possible future evolution of ERDO* [online], Journal of Energy Technology, Vol. 9, Iss. 1, p.p. 39 – 50, 2016. Available: http://www.fe.um.si/images/jet /Volume 9_Issue1/03-JET_marec_2016-PREPARATION_OF_NATIONAL.pdf (7. 10. 2016)

Example of reference-1 citation: In text *[1],* text continue.

Nomenclature

(Symbols)	(Symbol meaning)
t	time

JET I Journal of Energy Technology I Vol. 14, Issue 2, November 2021 I University of Maribor, Faculty of Energy Technology

ISSN 1855-5748

9 771855 574008